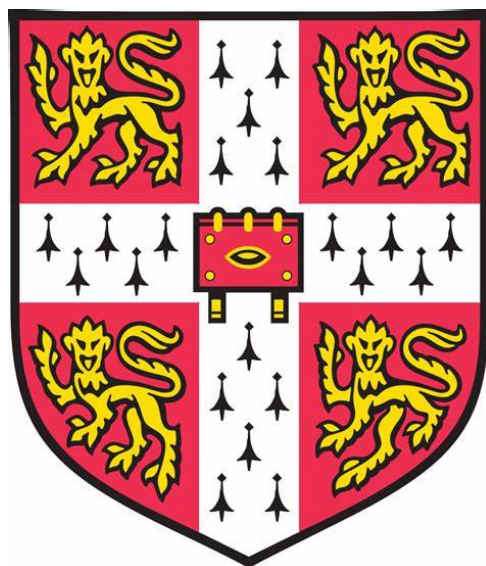


H₂ Production Prototype and Reverse Water Gas Shift



Joseph Jolley

Department of Engineering

Professor Stuart Scott

University of Cambridge

This dissertation is submitted for the Degree of Master of
Philosophy in Energy Technologies

Homerton College

23rd August 2024

Declaration

I hereby declare that except where specific reference is made to the work of others, the contents of this dissertation are the original and have not been submitted in whole or in any part for any other degree or qualification in this, or any other university. This dissertation is my own work and contains nothing which is the outcome of work done in collaboration with others, except as specified in the test and Acknowledgements. This dissertation contains 14,500 words excluding appendices, bibliography, footnotes, tables and equations and has fewer than 65 figures.

Joseph Jolley August 2024.

Abstract

This project provides a detailed investigation into various oxygen carrier materials for chemical looping hydrogen production purposes, tested through the cyclic reverse water gas shift reaction, which served as a proxy. The oxygen carriers tested in this project include (pelletised): Fe_2O_3 , $\text{SrFeO}_{3-\delta}$, 10wt% KOH/ $\text{SrFeO}_{3-\delta}$, $\text{LaFeO}_{3-\delta}$, 10wt% KOH/ $\text{LaFeO}_{3-\delta}$, 1 $\text{LaFeO}_{3-\delta}$:9 Fe_2O_3 , and 10wt% KOH/1 $\text{LaFeO}_{3-\delta}$:9 Fe_2O_3 . Perovskite oxygen carriers were produced through solid state synthesis, and the KOH pellets were doped through wet impregnation. The characterisation and phase identification of the oxygen carriers were completed through the use of powdered X-ray diffraction with Rietveld Refinement. Iron oxide and alternative oxygen carriers pellets were found to have a H_2 producing ability at 400°C, from using a thermogravimetric analyser, with Fe_2O_3 achieving the greatest redox capacity. The use of the reverse water gas shift reaction serving as a proxy for chemical looping hydrogen production was found to have potential flaws, in particular when testing with KOH doped oxygen carriers. Experiments were completed in a packed bed reactor with 113g of 1 $\text{LaFeO}_{3-\delta}$:9 Fe_2O_3 to test the scalability of the technology.

Contents

1	Introduction, Aims and Objectives	18
1.1	Introduction	18
1.2	Aim(s) and Objectives	26
1.2.1	Aim(s)	26
1.2.2	Objectives	26
2	Preliminary Modelling and Results	27
2.1	Iron Oxide Phase Diagram	27
2.2	Reducing Potential of Industrial Wastes (and alternatives)	29
3	Methodology	31
3.1	Material Preparation	31
3.2	Material Characterisation - XRD and Rietveld Refinement	34
3.3	Thermogravimetric Analysis	35
3.4	Scanning Electron Microscope	39
3.5	Packed Bed Reactor	39
3.5.1	Reactor Set Up, Gas Injection Schedule, Exhaust Analysis	39
4	Results	41
4.1	Phase Identification	41
4.1.1	$\text{La}_{0.5}\text{Sr}_{0.5}\text{FeO}_{3-\delta}$	41
4.1.2	$\text{LaFeO}_{3-\delta}$	42
4.1.3	$\text{SrFeO}_{3-\delta}$	43
4.1.4	KOH Doped Oxygen Carriers	43

4.2 TGA Results	47
4.2.1 Fe ₂ O ₃ Pellet vs Fe ₂ O ₃ Powder	47
4.2.2 SrFeO _{3-δ} Pellet vs 10 wt% KOH/SrFeO _{3-δ} Pellet	52
4.2.3 LaFeO _{3-δ} Pellet vs 10 wt% KOH/LaFeO _{3-δ} Pellet	57
4.2.4 1LaFeO _{3-δ} :9Fe ₂ O ₃ Pellet vs 10wt% KOH/1LaFeO _{3-δ} :9Fe ₂ O ₃ Pellet	61
4.3 Packed Bed Reactor	65
5 Limitations and considerations of the RWGS proxy for H₂ Production Testing	68
6 Conclusion	69
A Mass Flow Controller Calibration Procedure	75

List of Figures

1	General face centered and body centered cubic structure [11].	21
2	Double perovskite, with 50:50 A site occupation by 2 differing cations, general face centered and body centered cubic structure. [11]	22
3	Evolution of $La_xSr_{1-x}FeO_{3-\delta}$ vs temperature in H_2 , N_2 and Air. (A) Scattering angle as a function of temperature (heating, then cooling down). (B) Scattering angle at $T_{initial}$, T_{max} , T_{final} . (C) Coalescence of the rhombohedral LSF (208) and (220) peaks into singular cubic LSF (220) during heating and cooling (apart from the Air environment). [14].	23
4	SEM of an iron oxide pellet OC after 5 redox cycles, with the formation of a porous centre and smooth surface. [16].	24
5	WGS partial pressure equilibrium constant ($\ln(k_p)$) as a function of temperature.	26
6	Fe-O phase diagram as a function of temperature and $\frac{P_{CO}}{P_{CO_2}}$ reducing potential.	28
7	Fe-O phase diagram, with the reducing potentials of Acetone, Glycerol, and Ethanol plotted as a function of temperature.	30
8	PBR Schematic for the H_2 production prototype.	40
9	XRD scan and rietveld refinement of $La_{0.5}Sr_{0.5}FeO_{3-\delta}$ sample.	41
10	(a) Zoomed peak inspection of the potential $La_{0.5}Sr_{0.5}FeO_{3-\delta}$ sample for $2\theta \in [56.0, 63.1]^\circ$. (b) Zoomed peak inspection of the potential $La_{0.5}Sr_{0.5}FeO_{3-\delta}$ sample for $2\theta \in [66.0, 73.0]^\circ$	42
11	XRD scan and Rietveld refinement of the $LaFeO_{3-\delta}$ sample.	42
12	XRD scan and Rietveld refinement of the $SrFeO_{3-\delta}$ sample.	43
13	(a) XRD zoomed peak comparison between $SrFeO_{3-\delta}$ and 10wt% KOH/ $SrFeO_{3-\delta}$ within the range $2\theta \in [33.0, 34.2]^\circ$. (b) XRD zoomed peak comparison between $SrFeO_{3-\delta}$ and 10wt% KOH/ $SrFeO_{3-\delta}$ within the range $2\theta \in [58.6, 60.2]^\circ$	45
14	(a) XRD zoomed peak comparison between $LaFeO_{3-\delta}$ and 10wt% KOH/ $LaFeO_{3-\delta}$ within the range $2\theta \in [32.3, 33.5]^\circ$. (b) XRD zoomed peak comparison between $LaFeO_{3-\delta}$ and 10wt% KOH/ $LaFeO_{3-\delta}$ within the range $2\theta \in [57.6, 58.7]^\circ$	45

15	(a) XRD zoomed peak comparison between $1\text{LaFeO}_{3-\delta}:9\text{Fe}_2\text{O}_3$ and 10wt% KOH/ $1\text{LaFeO}_{3-\delta}:9\text{Fe}_2\text{O}_3$ within the range $2\theta \in [33.5, 34.4]^\circ$. (b) XRD zoomed peak comparison between $\text{LaFeO}_{3-\delta}$ and 10wt% KOH/ $\text{LaFeO}_{3-\delta}$ within the range $2\theta \in [36.0, 37.2]^\circ$	46
16	SEM scans for 10wt% KOH/ $\text{SrFeO}_{3-\delta}$	46
17	TGA cycles for the Fe_2O_3 Pellet sample (a) and Powder sample (b).	47
18	400°C isothermal reduction relative mass losses for (a) Fe_2O_3 Pellet and (b) Fe_2O_3 Powder.	48
19	500°C isothermal reduction relative mass losses for (a) Fe_2O_3 Pellet and (b) Fe_2O_3 Powder.	49
20	600°C isothermal reduction relative mass losses for (a) Fe_2O_3 Pellet and (b) Fe_2O_3 Powder.	49
21	Activation Energy (kJ/mol) comparison of Fe_2O_3 pellet and Fe_2O_3 powder, as a function of relative mass loss (%).	51
22	TGA cycles for (a) $\text{SrFeO}_{3-\delta}$ Pellet and (b) 10wt% KOH/ $\text{SrFeO}_{3-\delta}$ Pellet.	52
23	400°C isotherm reduction relative mass loss curves for (a) $\text{SrFeO}_{3-\delta}$ (b) 10 wt% KOH/ $\text{SrFeO}_{3-\delta}$	53
24	500°C isotherm reduction relative mass loss curves for (a) $\text{SrFeO}_{3-\delta}$ (b) 10 wt% KOH/ $\text{SrFeO}_{3-\delta}$	53
25	600°C isotherm reduction relative mass loss curves for (a) $\text{SrFeO}_{3-\delta}$ (b) 10 wt% KOH/ $\text{SrFeO}_{3-\delta}$	54
26	Activation Energy (kJ/mol) comparison of $\text{SrFeO}_{3-\delta}$ and 10wt% KOH/ $\text{SrFeO}_{3-\delta}$ pellets as a function of relative mass loss (%).	56
27	TGA cycles for (a) $\text{LaFeO}_{3-\delta}$ Pellet and (b) 10wt% $\text{LaFeO}_{3-\delta}$ Pellet. 4 redox cycle per isotherm: 300°C, 400°C, 500°C and 600°C	57
28	400°C isotherm reduction conversion curves for (a) $\text{LaFeO}_{3-\delta}$ (b) 10 wt% KOH/ $\text{LaFeO}_{3-\delta}$	58
29	500°C isotherm reduction conversion curves for (a) $\text{LaFeO}_{3-\delta}$ (b) 10 wt% KOH/ $\text{LaFeO}_{3-\delta}$	58
30	600°C isotherm reduction conversion curves for (a) $\text{LaFeO}_{3-\delta}$ (b) 10 wt% KOH/ $\text{LaFeO}_{3-\delta}$	59

31	Activation Energy (kJ/mol) comparison of LaFeO _{3-δ} and 10wt% KOH/LaFeO _{3-δ} pellets as a function of relative mass loss (%).	61
32	TGA cycles for (a) 1LaFeO _{3-δ} :9Fe ₂ O ₃ Pellet and (b) 10wt% 1LaFeO _{3-δ} :9Fe ₂ O ₃ Pellet.	61
33	400°C isotherm reduction conversion curves for (a) 1LaFeO _{3-δ} :9Fe ₂ O ₃ (b) 10 wt% KOH/1LaFeO _{3-δ} :9Fe ₂ O ₃	62
34	500°C isotherm reduction relative mass loss curves for (a) 1LaFeO _{3-δ} :9Fe ₂ O ₃ (b) 10 wt% KOH/1LaFeO _{3-δ} :9Fe ₂ O ₃	63
35	600°C isotherm reduction relative mass loss curves for (a) 1LaFeO _{3-δ} :9Fe ₂ O ₃ (b) 10 wt% KOH/1LaFeO _{3-δ} :9Fe ₂ O ₃	63
36	Activation Energy (kJ/mol) comparison of 1LaFeO _{3-δ} :9Fe ₂ O ₃ and 10wt% KOH/ 1LaFeO _{3-δ} :9Fe ₂ O ₃ pellets as a function of relative mass loss (%).	65
37	PBR at 490°C bed temperature and P=1atm. 113.19g of 1LaFeO _{3-δ} :9Fe ₂ O ₃ oxygen carrier. 5% H ₂ is the reducing agent. CO ₂ is the oxidising agent. Exhaust gas composition measured using the ABB EL3020, specifically for species; CO ₂ , CO, H ₂	66
38	Example of a equilibrium gradient within the PBR, where the OC does not redox homogeneously.	67

List of Tables

1	Iron Oxide Reduction - Relative Mass Losses	20
2	Doped Fe ₂ O ₃ and Fe ₃ O ₄ E _{vac} s. [8]	20
3	Fe-O phase transitions and their balanced redox reactions.	28
4	Pellet properties for Fe ₂ O ₃ , LaFeO _{3-δ} , 10wt% KOH/LaFeO _{3-δ} , SrFeO _{3-δ} , 10wt% KOH/SrFeO _{3-δ} , 1LaFeO _{3-δ} :9Fe ₂ O ₃ , 10wt% KOH/ 1LaFeO _{3-δ} :9Fe ₂ O ₃	33
5	Gas Stream Sequence for PBR Operation	40
6	Fe ₂ O ₃ pellet thiele moduli at the start of the reduction cycle (t=0s) and at the end of the reduction cycle (t=2400s) for the 400°C, 500°C and 600°C isotherms.	50
7	SrFeO _{3-δ} pellet thiele moduli at the start of the reduction cycle (t=0s) and at the end of the reduction cycle (t=2400s) for the 400°C, 500°C and 600°C isotherms.	55
8	LaFeO _{3-δ} pellet thiele moduli at the start of the reduction cycle (t=0s) and at the end of the reduction cycle (t=2400s) for the 400°C, 500°C and 600°C isotherms.	59
9	1LaFeO _{3-δ} :9Fe ₂ O ₃ pellet thiele moduli at the start of the reduction cycle (t=0s) and at the end of the reduction cycle (t=2400s) for the 400°C, 500°C and 600°C isotherms.	64
A1	Measured errors for the gas flow controllers represented by 2 standard deviations.	76

Nomenclature and Abbreviations

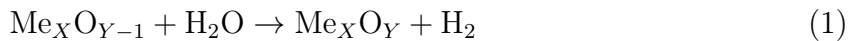
A	Pre-exponential Factor (s^{-1})
C	Concentration ($\frac{mol}{m^3}$)
CuK_{α}	Copper X-ray Radiation - L \rightarrow K shell (1.54Å)
CuK_{β}	Copper X-ray Radiation - M \rightarrow K shell (1.39Å)
C_2H_5H	Ethanol
C_3H_6O	Acetone
C_3H_8OH	Glycerol
CIF	Crystallography Information File
CL	Chemical Looping
$CLAS$	Chemical Looping Air Separation
$CLHP$	Chemical Looping Hydrogen Production
C_p	Constant Pressure Heat Capacity ($\frac{J}{molK}$)
DFT	Density Field Theory
D_{mol}	Molecular Diffusivity $\frac{m^2}{s}$
D_{eff}	Effective Diffusivity $\frac{m^2}{s}$
E_a	Activation Energy ($\frac{kJ}{mol}$)
E_{vac}	Surface Oxygen Vacancy of Formation Energy (eV)
EDS	Energy Dispersive Spectrometry
Fe	Elemental Iron
FeO	Wustite
Fe_3O_4	Magnetite
Fe_2O_3	Hematite
K_v	Volumetric Rate of Reaction (s^{-1})
KOH	Potassium Hydroxide
K_p	Partial Pressure Equilibrium Constant
MAE	Mean Absolute Error
m_i	Initial Mass of Oxygen Carrier, Before Reaction (g, mg, kg)
m_f	Final Mass of Oxygen Carrier, End of Reaction (g, mg, kg)
m^t	Mass During Reaction at Time 't' of Reaction (g, mg, kg)
mr_i	Molar Mass of Species 'i' ($\frac{g}{mol}$)
MFC	Mass Flow Controller
P	Pressure (atm or Pa)
PBR	Packed Bed Reactor
$r_{measure}$	Rate of O ₂ Moles Released ($\frac{mol}{s}$)
R	Universal Gas Constant = 8.314 $JK^{-1}mol^{-1}$
R_p	Radius of Cylindrical Pellet (m)
$RWGS$	Reverse Water Gas Shift
SED	Secondary Electron Detector

<i>SEM</i>	Scanning Electron Microscope
<i>SMR</i>	Steam Methane Reforming
<i>SSS</i>	Solid State Synthesis
<i>OC</i>	Oxygen Carrier
<i>T</i>	Temperature (K)
<i>TC</i>	k-rated Thermocouple
<i>TGA</i>	Thermogravimetric Analyser/Analysis
$\dot{V}_{\text{flow},i}$	Volumetric Flow Rate of Species 'i' ($\frac{\text{m}^3}{\text{second}}$)
<i>WGS</i>	Water Gas Shift
x_i	Mole Fraction of Species 'i'
<i>XRD</i>	X-ray Diffraction
δ	O_2 Non-stoichiometry
λ	Wavelength (m)
$d_{h,k,l}$	Planar Spacing of Crystal Structure
ρ_i	Density of Species 'i' (NTP) ($\frac{\text{g}}{\text{m}^3}$)
ϵ	Porosity of Pellet
2θ	Bragg Angle (°)
τ	Tortuosity
η	Effectiveness Factor
ϕ	Thiele Modulus

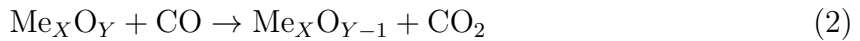
1. Introduction, Aims and Objectives

1.1 Introduction

Chemical Looping Hydrogen Production (CLHP) is a subcategory within Chemical Looping (CL). CL involves the use of redox reactions, with an oxygen carrier (OC) that transfers oxygen from an oxidising agent to a reducing agent, without the oxidising or reducing agents ever coming into direct contact. CLHP makes use of an OC, which first experiences reduction with a reducing agent, and then oxidises with H₂O. The oxidation reaction of an OC for a metal is given in the following form (specifically for CLHP):



The reduction of a metal OC with CO is represented in the following form:



Traditional reducing agent examples include hydrocarbons, and CO. A key benefit for the avoidance of the oxidising gas and reducing gas directly reacting (via the use of an OC), is to avoid an energy intensive downstream gas separation process. An example of a direct reaction is the reforming of steam-methane, where the reformer reaction is:



The carbon monoxide present as a product gas from the reformer can be further used in a downstream Water Gas Shift (WGS) reaction, by reacting with excess H₂O to produce further H₂. But the separation of CO₂ from the H₂ stream requires an additional work input. Currently Steam Methane Reforming is the most popular form of H₂ production, with approximately 95% of all H₂ production, coming from SMR with the remainder coming from alternative processes, including electrolysis [1].

This project takes a different path for H₂ production, using CL principles. This includes the manufacturing of OCs and a bed reactor to produce an exhaust stream containing H₂ (on a cyclic basis from a packed bed reactor, or a continuous basis using a fluidised bed reactor).

CLHP is not a new topic, these processes date back to 1908 where Lane [2] makes use of iron oxide as an OC to react with carbon monoxide (CO) to form reduced iron oxide, and

then oxidising the reduced iron oxide with steam (H_2O) to produce H_2 . CO and H_2 would be sourced from the gasification of coal. Messerschmitt [3] developed the technology by simplifying the process to only utilising a single retort, making H_2 production cheaper in 1910. Reed and Berg [4] patented an improved CLHP technology which made use of interlinked fluidised beds, whilst still making use of the iron oxide OC, this technology again was economically favourable in the early 1900s.

The Lane [2], Messerschmitt [3] and Reed and Berg [4] CLHP processes made use of the iron oxide phase change between Wusitie (FeO) and Hematite (Fe_3O_4) through the following reactions:

Iron oxide - reduction:



Iron oxide - oxidation:



There are 2 primary reactor designs which have been established over the past 2 centuries, including the packed bed and fluidised bed reactor. Packed bed reactors hold the OCs in place, and the inlet gas feed is alternated between the reducing, purging, oxidising and regeneration gases (suitable for batch production), the fluidised bed makes use of the circulation of OCs between different reactors (reducer, and re-oxidiser) which allow for continuous gas inlet streams (suitable for continuous production).

High temperature redox reactions of iron oxide can result in the sintering and agglomeration of iron particles, degrading redox performance [5]. Sintering degrades the redox potential of an OC by altering the composition of the crystal structure which is crucial to the reaction mechanisms [5]. Key properties of a good OC include negligible carbon deposition, negligible sintering and agglomeration during repeated redox reactions, and a significant lattice oxygen transfer ability [6]. Iron oxide based oxygen carriers have a key advantage of being rich in lattice oxygen and processing a range of oxidation states, including (ordered from the most oxidised, to the most reduced phase): Hematite (Fe_2O_3), Magnetite (Fe_3O_4), Wustite (FeO) and Elemental Iron (Fe) [7]. The mass losses (wt%) for the reduction reactions for the Fe-O phase transitions are shown in Table 1.

Table 1: Iron Oxide Reduction - Relative Mass Losses

Phase Reductions	Relative Mass Loss (wt%)
$\text{Fe}_2\text{O}_3 \rightarrow \text{Fe}_3\text{O}_4$	3.34
$\text{Fe}_3\text{O}_4 \rightarrow \text{FeO}$	6.91
$\text{FeO} \rightarrow \text{Fe}$	22.28

Material doping of OCs can modify their redox reaction kinetics, making them more favourable for H_2 production. They become more favourable due to 1. Improved reactivity 2. Improved recoverability, largely due to the reduced surface oxygen vacancy formation energy (the energy required to form a surface oxygen vacancy) [7]. The 'surface oxygen vacancy formation energy' (E_{vac}) is a measurement for describing the binding strength of the surface oxygen to a specific material [8]. Feng et al. [8], using Density Field Theory (DFT) calculated a standard for the E_{vac} of Fe_2O_3 to be 2.01 eV, and the E_{vac} of Fe_3O_4 to be 3.70 eV, proving that Fe_2O_3 has better ease of reducibility than Fe_3O_4 , as expected. Examples of various dopants for OCs include; lithium (Li), sodium (Na), potassium (K), magnesium (Mg), copper (Cu), lanthanum (La), and others. These dopants added to Fe_2O_3 and Fe_3O_4 (the wt% doping was not specified in the literature) were tested for their improved E_{vac} values, the calculated E_{vac} s are displayed in Table 2 below.

 Table 2: Doped Fe_2O_3 and Fe_3O_4 E_{vac} s. [8]

Dopant	E_{vac} - Fe_2O_3 (eV)	E_{vac} - Fe_3O_4 (eV)
Undoped	2.01	3.70
Li	1.39	3.49
Na	1.08	3.41
K	1.31	3.46
Mg	1.56	2.98
Cu	1.21	3.13
La	1.55	2.25
Ca	1.10	4.16

Green represents a reduced E_{vac} from the standard.

Red represents an increased E_{vac} from the standard.

As a result doping is proven to be advantageous when improving the reducibility kinetics (reducing the E_{vac} of surface oxygen binding) for Fe_2O_3 and Fe_3O_4 . Yet issues of sintering and agglomeration of iron oxide are reported to have remained [5]. Consequently this project will research alternative OC materials besides iron oxide.

Perovskite OCs have received interest in several fields of CL, including chemical looping combustion, chemical looping partial oxidation, chemical looping air separation, chemical looping hydrogen production, and others [7]. This project will focus on making use of perovskite structures. They are classified with the following molecular formula: ABX_3 , A and B are cations (of differing charge) and X is an anion which bonds to the cations

[9]. The perovskites considered within this project and CLHP are in the common form of $\text{ABO}_3-\delta$, where A is an alkaline (or rare earth) metal and B is a transition metal, with an example being Strontium Ferrite (SrFeO_3), with $\delta = 0$, representing the ideal stoichiometry. The addition of an alkaline metal ‘A’ affects the structural bonding arrangement between the transition metal and oxygen, which will change the concentrations of lattice oxygen and reducibility kinetics [7]. δ represents the non-stoichiometry of the perovskite structure. The δ can also change as a result of the oxygen partial pressure (P_{O_2}) and temperature (T), without a change occurring in the crystal structure of the perovskite [10]. 2 key disadvantages associated with perovskites include 1. Low mass of oxygen transferred per unit mass of perovskite 2. Some perovskites make use of toxic materials, and expensive materials e.g. Lanthanum [10]. Figure 1 shows the general cubic unit cell structure for a perovskite (note, not all perovskites follow a cubic crystal structure, others include; Orthorhombic, Rhombohedral, and more).

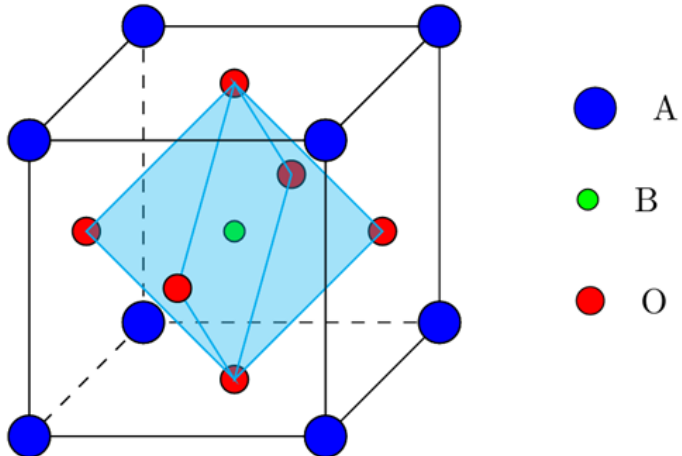


Figure 1: General face centered and body centered cubic structure [11].

Besides the traditional perovskite cubic structure displayed in Figure 1 above, there are variations that also exist, one is known as the ‘Double Perovskite’, where an additional (yet different type of) cation can occupy either the A or B site [9]. An example with an ideal stoichiometry being $\text{La}_{0.5}\text{Sr}_{0.5}\text{FeO}_3$. Double perovskites have been well researched and were identified to have good oxygen ion diffusion rates along with a well ordered structural arrangement resulting in good stability under multiple redox cycles (stable for 500 cycles for CLAS TGA Capstick et al. [12], 10 000 cycles for CLAS bench scale test Krizhevsky, Sutskever and Hinton [13], and 1000 cycles for CLAS TGA Görke et al. [10]), with a strong lattice structure with minimal distortion [9]. A general (cubic) crystal structure for a double perovskite is shown in Figure 2, with the certain A cation sites being occupied by A’ cations.

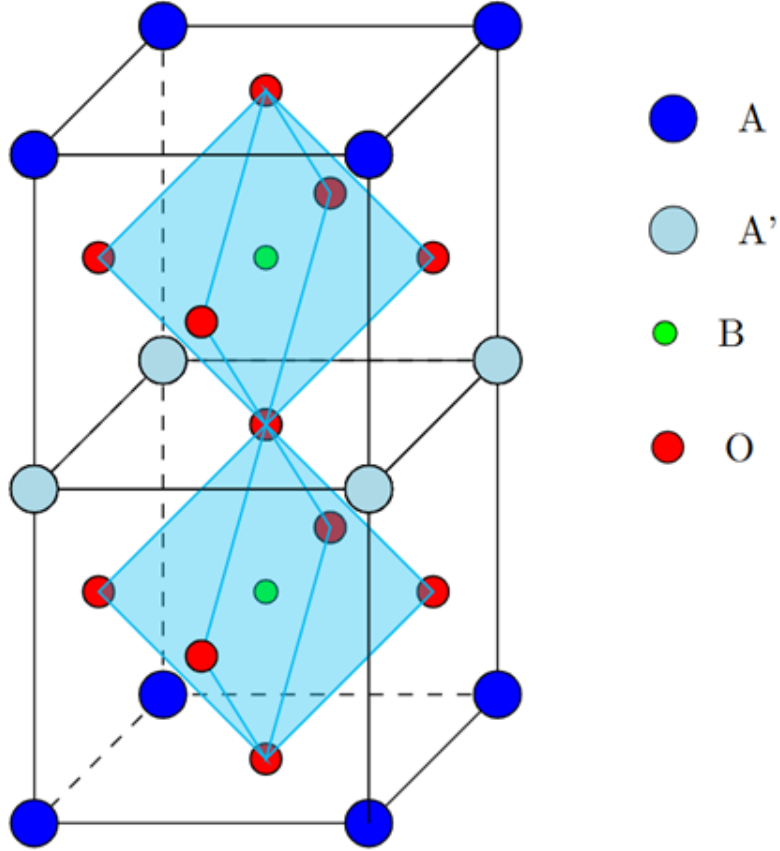


Figure 2: Double perovskite, with 50:50 A site occupation by 2 differing cations, general face centered and body centered cubic structure. [11]

$\text{La}_x\text{Sr}_{1-x}\text{FeO}_{3-\delta}$ can exist in distinct crystal structures, including rhombohedral ($\text{R}3\bar{c}$) and cubic ($\text{Pm}3\bar{m}$) [14]. It exists as a rhombohedral crystal structure, when the sample is placed under a reducing environment (H_2) and with an increased temperature greater than 673K, a non-linear shift in the scattering angle occurs, where the transitioned scattering angle now represents a cubic structure with a $\text{Pm}3\bar{m}$ space group (Figure 3 (a)) [14]. The linear shift in scattering angles can be explained by the thermal expansion due to the progressive temperature increase, with the unit cell constants and planar spacing's increasing, resulting in a decreasing Bragg angle. The inverse relationship between the crystal planar spacing ($d_{h,k,l}$) and Bragg angle (θ) is shown through Braggs Law (Equation 6):

$$\lambda = 2d_{h,k,l} \sin(\theta) \quad (6)$$

Upon cooling the $\text{La}_x\text{Sr}_{1-x}\text{FeO}_{3-\delta}$ perovskite (still in a H_2 reducing environment), the scattering angle increases in a linear manner, due to the reverse effect of thermal expansion, when cooling back to $T=293.15\text{K}$. Interestingly, the final scattering angle is not equal to the initial scattering angle, suggesting an irreversible crystal structure transition from rhombohedral to cubic (this procedure was carried out under a reducing environment) [14].

Testing if the crystal structure of $\text{La}_x\text{Sr}_{1-x}\text{FeO}_3$ reverts back from cubic to rhombohedral upon cooling and in an oxidative environment was not reported. If cooling in an oxidiative environment was tested, it is expected that the original rhombohedral ($\text{R}3\bar{c}$) structure would have been recovered. Heating $\text{La}_x\text{Sr}_{1-x}\text{FeO}_3$ from 293K to 873K under an oxidising environment, and then cooling back to 293K showed only a linear shift in the scattering angle, with no non-linear shift present, the initial scattering angle is also equal to the final scattering angle, therefore retaining the rhombohedral structure [14].

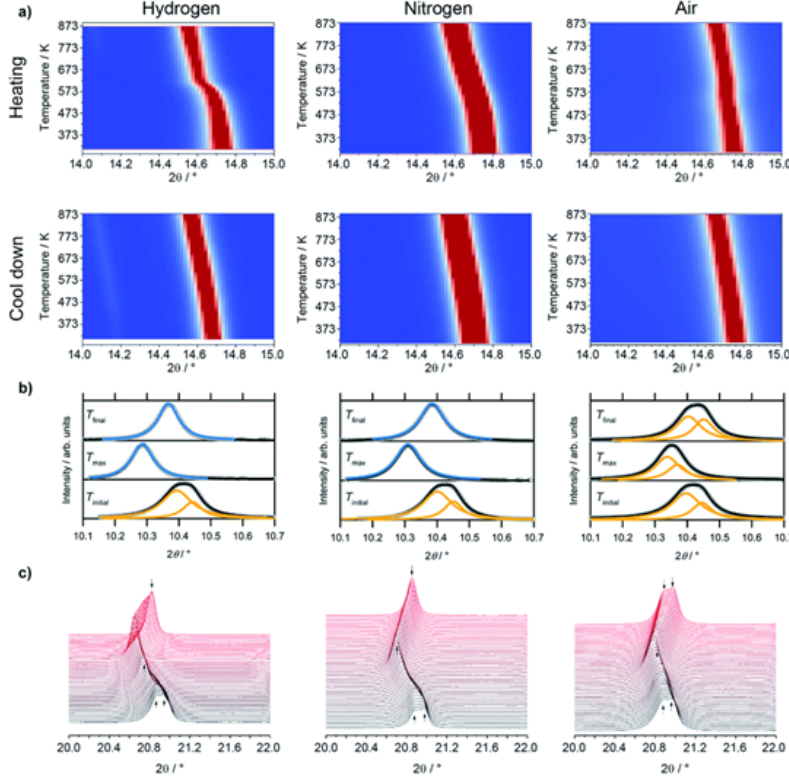


Figure 3: Evolution of $\text{La}_x\text{Sr}_{1-x}\text{FeO}_{3-\delta}$ vs temperature in H_2 , N_2 and Air. (A) Scattering angle as a function of temperature (heating, then cooling down). (B) Scattering angle at $T_{initial}$, T_{max} , T_{final} . (C) Coalescence of the rhombohedral LSF (208) and (220) peaks into singular cubic LSF (220) during heating and cooling (apart from the Air environment). [14].

In the domain of CL, the primary incentives towards selecting suitable OC solids include cost, stability and abundance. Perovskites, such as $\text{SrFeO}_{3-\delta}$, have demonstrated stable durability across 30 redox reaction cycles [15]. Additionally $\text{SrFeO}_{3-\delta}$ can release oxygen at temperatures as low as 400°C, even in the presence of air (with high P_{O_2}) [15]. In contrast to perovskites, iron oxide is prone to sintering and a decreasing surface area after several redox cycles at high temperatures. In particular, the reduced phases of iron oxide (FeO, Fe) are more prone to sintering and agglomeration, leading to a significantly reduced O_2 transfer ability [16]. Upon deep reduction and oxidation, the iron oxide experiences the formation of a porous centre, whereby the Fe^{2+} and Fe^{3+} cations diffused outwards at a greater rate than the inward diffusing O^{2-} anions, this imbalanced diffusion (Kirkendall effect) leads to the formation of voids, which can result in a reduced structural integrity

(weaker crushing strength), rendering them unsuitable for certain chemical looping applications [16]. Figure 4 shows iron oxide being used as an oxygen carrier, and after 5 redox cycles (at 800°C at atmospheric pressure) there is a void formation and smooth surface present.

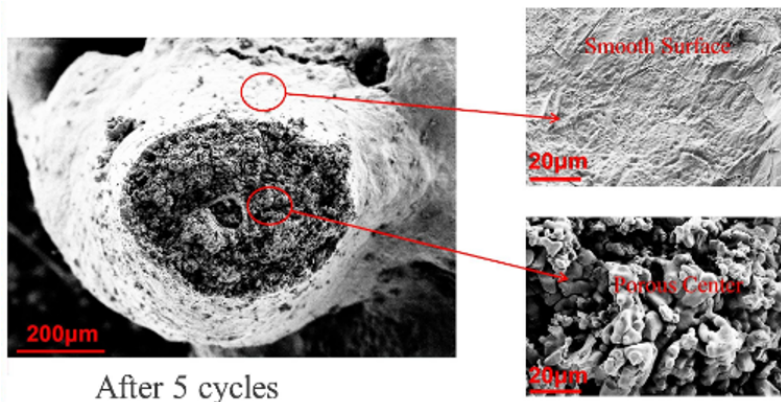


Figure 4: SEM of an iron oxide pellet OC after 5 redox cycles, with the formation of a porous centre and smooth surface. [16].

Sintering occurs more often at high temperatures (near the Taman temperature), during sintering the surface grains grow and the surface area can decrease, hence reducing the reactivity of the OC by the blocked pores [17]. Difficulties in lattice O₂ transfer can also occur due to distance for O₂ transmission increasing also as a result of sintering [17]. Perovskites such as SrFeO_{3-δ} and LaFeO_{3-δ} have two varieties of O₂ associated with it. 1. Surface bound O₂ 2. Lattice O₂, with the surface O₂ being highly reactive and useful in oxidation reactions, and the lattice O₂ being associated with greater volumes of O₂ transfer from within the bulk material [9]. Whilst doping of iron oxide was proven to improve redox kinetics by Feng et al. [8], doping can also be applied to perovskites with the aim of not only to improve the redox kinetics of O₂ transfer, but also to improve the general stability (e.g. resistance to sintering, carbon formation and deposition) [9].

The additive Al₂O₃ has been reported to improve the redox stability of the iron based OCs, however deeply reduced iron oxide (beyond FeO) with Al₂O₃ support has been reported to form FeAl₂O₄ (hercynite) which is known to be an inert substance, hence limiting the redox potential [18]. When deciding on suitable additives to act as support, literature research should be done prior to practical testing to determine the feasibility.

Zirconia has been proposed as an additive with iron oxide in the form of: 30wt% ZrO₂/Fe-O, which resulted in 90% hydrogen yield from 20 redox cycles whilst maintaining a stable structure [18]. 10 redox cycles of 20wt% Fe₂O₃/ZrO₂ at 750°C resulted in only slight sintering provided, as deep reduction was avoided and stopped at FeO [18]. Reducing to Fe resulted in the previously discussed Kirkendall effect taking place, with iron ions moving to the outer regions of the particle, forming a smooth surface and consequently reducing the H₂ yield [18].

Alcohols have been proposed as reducing agents, such as bio-ethanol [19]. When using a carbonaceous containing species as a reducing agent, it was found that carbon formation on the OC surface is possible under certain operating conditions [19]. Two proposals were also made to mitigate for carbon formation, including 1. using redox cycles with shortened exposure times to the reducing and oxidising agents (high frequencies for gas transitions) can minimise the carbon contamination of the OC. 2. a regular cycle in air at elevated, can help regenerate the OC [18]. De Filippis et al. [19] also concluded that coke deposition is largely dependent on the reduction period. De Filippis et al. [19] operated a fixed bed reactor and tested a range of reduction periods ranging from 7 minutes ($5 \text{ mmol}_{\text{C}_2\text{H}_5\text{OH}}/\text{g}_{\text{Fe}_2\text{O}_3}$) - 25 minutes ($17.95 \text{ mmol}_{\text{C}_2\text{H}_5\text{OH}}/\text{g}_{\text{Fe}_2\text{O}_3}$) for carbon deposition (reactor conditions: $T = 675^\circ\text{C}$ and $P = 1\text{atm}$). 7 minutes of ethanol injection was optimal for inhibiting coke deposition, as for the injection periods of 9 minutes and 25 minutes, carbonaceous species were present in the exhaust stream during oxidisation in H_2O , leading to a contaminated stream of H_2 [19]. This suggests that carbon deposition must have occurred during the prolonged reduction phases in ethanol [19]. A consequence of using low injection periods of $\text{C}_2\text{H}_5\text{OH}$ will consequently reduce the H_2 yield per redox cycle, due to the lack of depth of reduction achieved.

Besides alcohols, alternative waste gases such as acetone ($\text{C}_3\text{H}_6\text{O}$) can also be used to reduce the OC for CLHP. However, for this project, cyclic Reverse Water Gas Shift (RWGS) will be used. The RWGS reaction is used because it can serve as a proxy for H_2 production, and to test the yield of CO production. The WGS reaction favours the formation of CO_2 and H_2 over CO and H_2O ($\ln(K_P) > 0$) (for the temperatures of interest in this project). Figure 5 shows the partial pressure WGS equilibrium constant varying with temperature. Therefore, when using CO_2 for oxidation, if the OC gains mass and produces CO, the OC is considered to be H_2 producing. The OC materials in this project will be first tested in a thermogravimetric analyser (TGA) using the cyclic RWGS to determine their mass loss in H_2 and mass gain in CO_2 . Furthermore cyclic RWGS will be tested on a larger scale packed bed reactor, to test the scalability of this technology. This research will serve as a foundation for future testing of materials for CLHP purposes. With suitable materials identified, the use of a carbonaceous waste species can be used to aid with the reduction step, whilst the oxidation step allows for the production of H_2 .

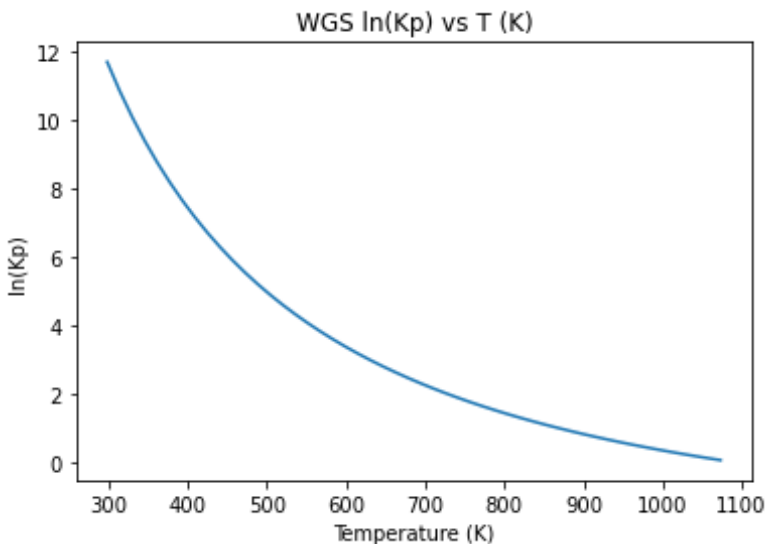


Figure 5: WGS partial pressure equilibrium constant ($\ln(k_p)$) as a function of temperature.

1.2 Aim(s) and Objectives

1.2.1 Aim(s)

To research oxygen carriers at low temperatures (<500°C) for a H₂ producing ability (using RWGS as a proxy), and operate RWGS redox cycles in a packed bed reactor to test the technology at greater scale.

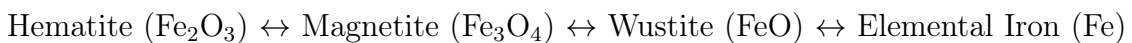
1.2.2 Objectives

- Complete a systematic literature review on the topic of Chemical Looping Hydrogen Production.
- Produce an Iron Oxide Phase diagram as a function of temperature and gas reducing potential.
- Produce perovskite pellets through Solid State Synthesis.
- Material characterisation of the sample perovskites using XRD with Rietveld Refinement (GSAS II software).
- Test sample pellets in a Thermogravimetric Analyser to test their basic thermochemical properties, through redox cycles using H₂ and CO₂ (cyclic RWGS).
- Set up the packed bed reactor operation.
- Test the packed bed reactor at scale using RWGS to test for larger scale H₂ capability.

2. Preliminary Modelling and Results

2.1 Iron Oxide Phase Diagram

An iron oxide (Fe-O) phase diagram shows what phase of iron-oxide should exist for a given temperature, and a given reducing potential. With the various phases of Fe-O, the reduction/oxidation of Fe-O takes a sequential path as suggested by an Fe-O phase diagram, however in certain circumstances this is not always true. The general transition of iron oxide starting from Hematite (most oxidised) to Elemental Iron (most reduced) is as follows:



Several reducing agents can be used to model the reduction of Fe-O, in this case, carbon monoxide (CO) will be used as the reducing agent. If an alternative reducing agent is used (e.g. ethanol), its equivalent reducing potential in terms of $P_{\text{CO}}/P_{\text{CO}_2}$ can be calculated, as the reducing potential (y-axis) of an Fe-O phase diagram is often plotted in terms of common gases, e.g. $P_{\text{CO}}/P_{\text{CO}_2}$ or $P_{\text{H}_2}/P_{\text{H}_2\text{O}}$.

The production of an Fe-O phase diagram, starts with the standard Gibbs energy of reaction, per mole of CO:

$$\Delta G = \Delta G^\circ + RT \ln(Q) \quad (7)$$

With Q being the general reaction quotient between the reactant and product gases. Upon reaching equilibrium $\Delta G = 0$ kJ/mol, the equation can be simplified to:

$$-\Delta G^\circ = RT \ln(Q) \quad (8)$$

A balanced Fe-O reaction can be re-formulated as follows to calculate the partial pressure ratio at equilibrium. Below is an example redox reaction between Hematite (Fe_2O_3) and Magnetite (Fe_3O_4).



$$-\Delta G^\circ = n_{\text{CO}}RT \ln(Q) \quad (10)$$

$$e^{\frac{-\Delta G^O}{nCO RT}} = \frac{P_{CO_2}}{P_{CO}} \quad (11)$$

This procedure was carried out for the redox reactions between each adjacent phase of Fe-O, Table 3 shows the balanced redox reactions for the Fe-O phases, with CO as the reducing agent, and CO₂ as the oxidising agent.

Table 3: Fe-O phase transitions and their balanced redox reactions.

Iron Phase Transition	Balanced Redox Reactions
Hematite \leftrightarrow Magnetite	$3Fe_2O_3(s) + CO(g) \leftrightarrow 2Fe_3O_4(s) + CO_2(g)$
Magnetite \leftrightarrow Wustite	$0.947Fe_3O_4(s) + 0.788CO(g) \leftrightarrow 3Fe0.947O_{(s)} + 0.788CO_2(g)$
Wustite \leftrightarrow Elemental Iron	$Fe0.947O_{(s)} + CO_{(g)} \leftrightarrow 0.947Fe_{(s)} + CO_2(g)$

For the reactions listed in Table 3, their equilibrium partial pressure ratios of P_{CO}/P_{CO_2} is a function of temperature, pressure, and number of moles for the reactant species (only stoichiometric reactions have been considered in Table 3). The modelled system pressure is constant at 101.325 kPa, with the gibbs energy data from the NASA CEA database [20].

These equilibrium partial pressure ratios act as boundaries, passing beyond one of these equilibrium bounds (due to strong reducing or oxidising potential) causes another phase of Fe-O to be formed. The P_{CO}/P_{CO_2} for each of the reducing reactions as a function of temperature, is plotted in Figure 6.

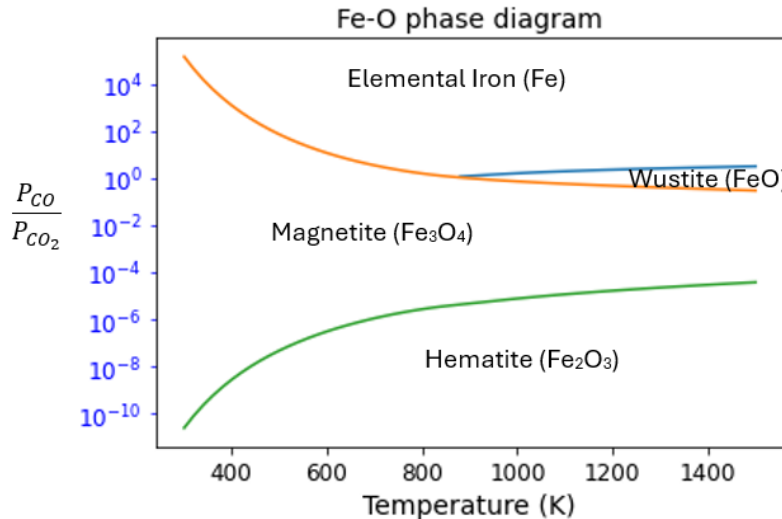


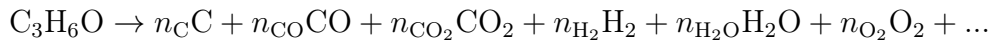
Figure 6: Fe-O phase diagram as a function of temperature and $\frac{P_{CO}}{P_{CO_2}}$ reducing potential.

2.2 Reducing Potential of Industrial Wastes (and alternatives)

With the Fe-O phase diagram plotted in terms of $\frac{P_{CO}}{P_{CO_2}}$, alternative reducing agents can be plotted on the Fe-O phase diagram to determine their reducing potentials at various temperatures. Alternative reducing agents include: Acetone (C_3H_6O), Ethanol (C_2H_6O), and Glycerol ($C_3H_8O_3$) and others. Each can combust with the oxygen from an OC e.g. iron oxide, to produce a reduced phase of iron oxide.

The modelling of acetone's reducing potential on an Fe-O phase diagram is achieved by (assuming its dissociation) dissociating acetone into fundamental species (CO_2 , CO , H_2 , H_2 , and O_2), and allowing the dissociated gas composition to reach a state of equilibrium (using the equilibrium constants method). Acetone's equivalent reducing potential in terms of $\frac{P_{CO}}{P_{CO_2}}$ can now be calculated as a function of temperature, and plotted onto the Fe-O phase diagram.

The following reaction shows the general dissociation of acetone (to determine its equivalent reducing potential):



The number of product gas moles for each species (n_i) will change with temperature, due to the equilibrium reaction constants being functions of temperature. The continuation '...' represents several other species, however this term is truncated to reduce the complexity of the nonlinear system, this is allowed because the partial pressures of these truncated species upon reaching equilibrium are negligible and have minimal effect on the final reducing potential calculated.

The steps for calculating the moles of the dissociated acetone constituents species, involve solving a non-linear system of moles balances and reaction constants for the Water Gas Shift (WGS) reaction, hydrogen combustion and the Boudouard reaction (only required at low temperatures to account for carbon formation). Additionally, the reducing potentials for glycerol and ethanol have been solved for in the same manner. Figure 7 shows their equivalent reducing potentials on the Fe-O phase diagram. Noticeably, acetone is higher on the Fe-O phase diagram than glycerol and ethanol, this is due to their chemical formulas of C_3H_6O (Acetone), $C_3H_8O_3$ (Glycerol) and C_2H_6O (Ethanol), whereby glycerol and ethanol have a greater oxygen:carbon ratio in contrast to acetone. With acetone having a lower oxygen:carbon ratio, it has a stronger reducing potential, and therefore the plot for acetone is shifted upwards on the Fe-O phase diagram for all T (in comparison to the plots for glycerol and ethanol). Acetone can also produce elemental iron at lower temperatures ($\sim 825\text{ K}$) in comparison to ethanol ($\sim 845\text{ K}$) and glycerol ($\sim 895\text{ K}$). Figure 7 shows that a reactant with a stronger reducing potential, has a greater ability to reduce at lower

temperatures in contrast to alternatives with weaker reducing potentials.

If a reactant has no oxygen molecules present (e.g. methane - CH_4), it is considered to be ‘infinitely’ reducing as it cannot be plotted on the Fe-O phase diagram. This is a result of no oxygen molecules being present to produce any of the product gases (CO_2 , H_2O , O_2) upon reaching its dissociated equilibrium. Without these species, their partial pressures including P_{O_2} and $\frac{P_{\text{CO}}}{P_{\text{CO}_2}}$ cannot be defined, and nor can the exact reducing potential, hence it is considered infinitely reducing.

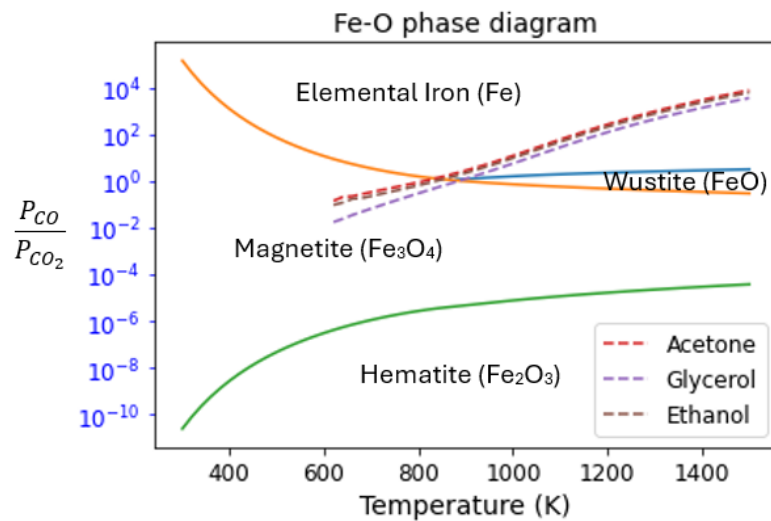


Figure 7: Fe-O phase diagram, with the reducing potentials of Acetone, Glycerol, and Ethanol plotted as a function of temperature.

3. Methodology

3.1 Material Preparation

3 key perovskite materials were sampled during this project including: LaFeO_{3-δ}, SrFeO_{3-δ}, and La_{0.5}Sr_{0.5}FeO_{3-δ}, all of which were produced through a solid state synthesis (SSS) manufacturing process.

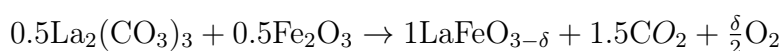
To produce LaFeO_{3-δ}, stoichiometric amounts of precursors including La₂(CO₃)₃ (~ 67.10 wt%, Alfa Aesar) with the 67.1 wt% purity (determined by TGA heating) being due to its significant hygroscopic nature, and Fe₂O₃ (>98 wt%, Fisher Chemical) were added in the following molar ratio 1.46 La₂(CO₃)₃ : 1 Fe₂O₃ (not 1:1 due to the H₂O hygroscopic absorption property of the La₂(CO₃)₃ precursor).

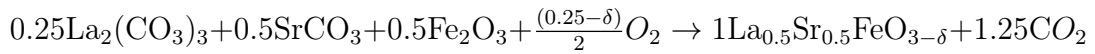
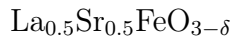
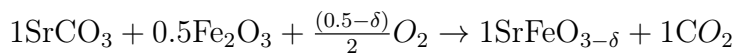
To produce SrFeO_{3-δ}, stoichiometric amounts of precursors including SrCO₃ (>98 wt% Sigma-Aldrich) and Fe₂O₃ (>98 wt% Fisher Chemical) were added in the following molar ratio 1SrCO₃ : 1Fe₂O₃.

To produce La_{0.5}Sr_{0.5}FeO_{3-δ}, stoichiometric amounts of precursors including La₂(CO₃)₃ (~ 67.10 wt%, Alfa Aesar), SrCO₃ (>98 wt% Sigma-Aldrich), and Fe₂O₃ (>98 wt% Fisher Chemical) were added in the following molar ratio, 1 La₂(CO₃)₃ : 1.369SrCO₃ : 1.369 Fe₂O₃ (also as a consequence of the hygroscopic nature of La₂(CO₃)₃).

To produce each of the perovskites at scale, the precursor powders were first manually mixed until reaching a homogeneous mixture, then the addition of ethanol (>99.8%, Sigma-Aldrich), at ~0.55ml/g of precursor powder was used as a binding agent. The precursor mix was then added to a ball mill mixer (MTI planetary ball mill mixer, MSK-SFM-1), and mixed for 6 cycles, each with 10 minutes active milling (at 25Hz) and 20 minutes rest, leading to a total of 60 minutes active milling. The mixture was then left at room temperature for the ethanol to evaporate for ~24 hours. The mixture was then checked, if any signs of a slurry-based mixture were shown then the mixture was left for several more hours, however 24 hours was often sufficient to dry the mixture.

The precursor mixture was then scraped from the mill into a crucible, and placed in a muffle furnace to operate at 1000°C for 6 hours, with a ramp rate of (5°C)/minute for calcination. Calcination of the 3 perovskite materials are shown by the following reactions (here assuming 100 wt% purity):





Another OC with a ratio of $1\text{LaFeO}_{3-\delta}:9\text{Fe}_2\text{O}_3$ was also produced. The mixture of $1\text{LaFeO}_{3-\delta}:9\text{Fe}_2\text{O}_3$ with ethanol (acting as mixing agent) (>99.8%, Sigma-Aldrich), at $\sim 0.55\text{ml/g}$ was added to the planetary ball mill, with 6 cycles of 10 minutes active milling. The sample was left in room temperature for 24 hours for the ethanol to evaporate. Then the sample was added to a crucible and placed in a muffle furnace at 900°C for 3 hours, and a ramp rate of $5^\circ\text{C}/\text{min}$.

With the above materials now synthesised, they were all (and Fe_2O_3) pelletised using an LFA TDP 0 pill press. After pressing, the shaped pellet is then reheated in the muffle furnace at 900°C for 3 hours. This muffle furnace cycle is crucial as the recently pressed sample does not have significant structural integrity, and needs to be re-fired. Pelletised samples were tested in a TGA rather than using powdered samples, this will gauge better expectations of a scaled packed bed performance. The average mass of a pellet produced is $\sim 116\text{mg}$.

A select few samples of key interest were also tested with potassium hydroxide (KOH) doping, these included: $\text{LaFeO}_{3-\delta}$, $\text{SrFeO}_{3-\delta}$, and $1\text{LaFeO}_{3-\delta}:9\text{Fe}_2\text{O}_3$. A process of wet impregnation was employed whereby a 7M concentrated solution of KOH was produced, as a result of the average porous volume of the pellet samples being recorded as low (porous volume data for each pellet is recorded in Table 4).

To determine the concentration of KOH solution for 10 wt% doping, measurements of deionized water absorption were taken for 8 pellets of each of the samples: $\text{LaFeO}_{3-\delta}$, $\text{SrFeO}_{3-\delta}$, and $1\text{LaFeO}_{3-\delta}:9\text{Fe}_2\text{O}_3$. This allowed for the calculation of the average porous volume of the pellets to be made. The average porous volumes (and standard deviations) are shown in Table 4 below. Based on these measurements, a 7M KOH solution was chosen. Whilst the Fe_2O_3 was not tested with KOH impregnation the porous volume was measured as $0.1989\text{ ml/g} \pm 0.0341\text{ ml/g}$. Pelletised samples would be doped in an excess solution of the 7M KOH solution. The pellet samples were then heated to 250°C at $5^\circ\text{C}/\text{min}$ to evaporate the water and to reform some structural integrity of the pellet, high calcination-like temperatures were avoided as that would result in melting and the possible evaporation of the KOH molecules. The true wt% KOH content was determined by weighing the pellet prior to the impregnation procedure, and then weighing the pellet

after the impregnation and heating at 250°C was completed, the mass increase would be associated with the wt% KOH content. With 10wt% KOH being the target doping, this was often not achieved as a result of the lack of control available from wet impregnation, and the singular pellets not having the exact average porous volume. Table 4 shows the target doping of KOH along with the actual doping of KOH achieved.

The experimental procedure discussed above for determining the porous volume of the pellets has weaknesses associated with it. Firstly, certain pores of the pellet will be associated with the capillary limit, where the pore is too small the surface tension cannot be overcome to allow water through (this will cause an underestimate of the true porous volume). Secondly, surface bound water which is not actually associated with porous volume (this will cause an overestimate of the true porous volume).

Key information of the pellets including; average mass, average porous volume, porosity, target KOH wt% and the achieved KOH wt% is shown in Table 4 below.

Table 4: Pellet properties for Fe_2O_3 , $\text{LaFeO}_{3-\delta}$, 10wt% KOH/ $\text{LaFeO}_{3-\delta}$, $\text{SrFeO}_{3-\delta}$, 10wt% KOH/ $\text{SrFeO}_{3-\delta}$, 1 $\text{LaFeO}_{3-\delta}$:9 Fe_2O_3 , 10wt% KOH/ 1 $\text{LaFeO}_{3-\delta}$:9 Fe_2O_3 .

Pellet Formula	Avg. Mass (mg)	Avg. Porous Vol (ml/g)	Porosity	Target KOH wt%	Achieved KOH wt%
Fe_2O_3^1	121	0.1989 ± 0.0341	0.00114	n.a	n.a
$\text{LaFeO}_{3-\delta}^1$	115	0.2536 ± 0.0110	0.00138	n.a	n.a
KOH/ $\text{LaFeO}_{3-\delta}^2$	127.4	n.a	n.a	10.0	10.8
$\text{SrFeO}_{3-\delta}^1$	109	0.2441 ± 0.0229	0.00126	n.a	n.a
KOH/ $\text{SrFeO}_{3-\delta}^2$	119.1	n.a	n.a	10.0	9.3
1 $\text{LaFeO}_{3-\delta}$:9 Fe_2O_3^1	122.0	0.2559 ± 0.0210	0.00147	n.a	n.a
KOH/ 1 $\text{LaFeO}_{3-\delta}$:9 Fe_2O_3^2	134.8	n.a	n.a	10.0	10.5

Footnote: The ± accounts for ±1 standard deviation (std). Average volume of a pellet produced in approximately 21.2ml. With the cylindrical radius of the pellet calculated to be 1.3mm (vernier calipers). n.a. refers to not applicable, the measurement was not taken as it was not required for the results or discussion.

¹ Data taken from an average of 8 pellets.

² Data taken from single doped pellet, hence no std data distribution.

3.2 Material Characterisation - XRD and Rietveld Refinement

Phase identification of the oxygen carrier samples produced from solid state synthesis was performed using powdered X-ray diffraction (XRD). PANalytical X’Pert Pro was used with $2\theta = 10\text{--}85^\circ$ and Cu K α radiation. Each XRD scan was operated with 35kV and 15mA, $\Delta\theta=0.002089^\circ$ with a corresponding time per step of $\Delta t=19.05\text{s}$ for a total scan time of 01:32:22 (h:m:s). Rietveld refinement was performed using GSAS II ([21]) whereby the observed sample data of the scan was compared to CIF files of known phases, and the CIF file was refined in an attempt to improve the fit. Key samples which were manufactured and tested through XRD include; LaFeO $_{3-\delta}$, 10wt% KOH/LaFeO $_{3-\delta}$, SrFeO $_{3-\delta}$, 10wt% KOH/SrFeO $_{3-\delta}$, La $_{0.5}$ Sr $_{0.5}$ FeO $_{3-\delta}$, 1LaFeO $_{3-\delta}$:9Fe $_2$ O $_3$, and 10wt% KOH/1LaFeO $_{3-\delta}$:9Fe $_2$ O $_3$.

XRD characterisation and Rietveld refinement allowed for the LaFeO $_{3-\delta}$ and 10wt% KOH/LaFeO $_{3-\delta}$ samples to be well fit to LaFeO $_3$ (ICSD 164083) (space group Pnma), alternative space groups of LaFeO $_3$ were trialled in an attempt to achieve a better fit, including: ICSD 236171 (space group R- $\tilde{3}c$) and ICSD 236153 (space group Pbnm), however they did not result in a better fit.

XRD characterisation and Rietveld refinement allowed the SrFeO $_{3-\delta}$ and 10wt% KOH/SrFeO $_{3-\delta}$ samples to be well fit by the SrFeO $_{3-\delta}$ (ICSD 91062) CIF file. Additional phases were also tested (in an attempt to account for non-stoichiometry), but they did not result in a better fit. These included: SrFeO $_{2.75}$ (ICSD 119281) and Sr $_2$ Fe $_2$ O $_5$ (ICSD 249008).

XRD characterisation and Rietveld refinement allowed the La $_{0.5}$ Sr $_{0.5}$ FeO $_{3-\delta}$ sample to be well fit by CIF files. However it is later shown in the Results section that there is a lack of phase purity present. The CIF files which improved the fit included: La $_{0.5}$ Sr $_{0.5}$ FeO $_{3-\delta}$ (ICSD 674775), LaFeO $_{3-\delta}$ (ICSD 164083), and SrFeO $_{3-\delta}$ (ICSD 91062). Additional CIF files were considered and tested for, but they did not improve the overall fit, including: La $_{0.4}$ Sr $_{0.6}$ FeO $_3$ (ICSD 78067), La $_{0.6}$ Sr $_{0.4}$ FeO $_3$ (ICSD 98069), La $_{0.6}$ Sr $_{0.4}$ FeO $_{2.8}$ (ICSD 98072), La $_{0.6}$ Sr $_{0.4}$ FeO $_{2.71}$ (ICSD 98074), Fe $_2$ O $_3$ (ICSD 15840), Fe (ICSD 185741), La $_2$ O $_3$ (ICSD 24693), SrFeO $_{2.75}$ (ICSD 119281), Sr $_2$ Fe $_2$ O $_5$ (ICSD 249008), and Sr $_3$ Fe $_2$ O $_7$ (ICSD 74422).

XRD characterisation and Rietveld refinement allowed the 1LaFeO $_{3-\delta}$:9Fe $_2$ O $_3$, and 10wt% KOH/1LaFeO $_{3-\delta}$:9Fe $_2$ O $_3$ samples to be fit by the LaFeO $_3$ (ICSD 164083) (space group Pnma) and the Fe $_2$ O $_3$ (ICSD 15840) CIF files.

3.3 Thermogravimetric Analysis

Thermogravimetric analysis (TGA) was used to characterise the basic redox properties of the oxygen carrier pellets. The TGA tests completed throughout this project used a TGA/DSC 1 Star System analyser with a horizontal reaction chamber. Alumina crucibles containing the testing samples were placed on a measured balance arm within the reaction chamber. The chamber operates with 50 ml/min from purge and protective gas streams of N₂ (>99.99% BOC Linde Group) at 20°C and 1 bar (all other gases mentioned were also measured at 20°C and 1 bar). During the TGA experiments, a variety of reactive gases were also used with an injection rate of 50 ml/min into the reaction chamber. The gases used include: Air, 5% H₂/N₂ (measured on a per mole basis), CO₂, and N₂ (inert) (>99.99 wt% BOC Linde Group). It is noted that the reactive gases used in the TGA experiments are roughly a third of their initial concentration due to dilution from the purge (N₂ 50 ml/min) and protective (N₂ 50 ml/min) gas streams. e.g. for H₂/N₂ the total flow rate is 150ml/min with 1.667% H₂ in N₂.

One type of TGA experiment was performed. Operating at 101.325 kPa, the samples were cycled at 4 isotherms (360min/isotherm), including: 300°C, 400°C, 500°, and 600°C with a ramp rate of 10°C/min. At each isotherm, the injection procedure was 2400 seconds of H₂ (5%), followed by 2400 seconds of CO₂ (x4), finishing with 2400 seconds in Air (corresponding to 360min/isotherm). During the dynamic heating between isotherms, Air was used. The initial heating to 300°C and final cooling from 600°C was also completed in Air.

TGA results are analysed through the relative mass loss curves during the reduction cycles, the relative mass loss during a reduction cycle of an OC at time 't' of H₂ injection is given by equation 12.

$$m_r^{(t)} = 1 - \frac{m_{\text{red}}^{(t)}}{m_{\text{red}}^{(t=0)}} \quad (12)$$

Where, $m_{\text{red}}^{(t)}$ is the mass of the OC during the reduction process at time t, t=0s represents the start of the reduction reaction between the OC and H₂.

The degree of a reaction can be determine through the 'conversion' which ranges from 0 (start of reaction) to 1 (end of reaction). The degree of conversion throughout a reaction is calculated by:

$$\text{Conversion}^{(t)} = \frac{m_i - m^{(t)}}{m_i - m_f} \quad (13)$$

Where $0 \leq \text{Conversion} \leq 1$, m_i represents the initial mass prior to the reaction, $m^{(t)}$ represents an intermediate mass during the reaction at a particular time 't', and m_f represents the final mass at the end of reaction.

The kinetics of the solid-gas reactions were modelled using an integral isomass concept, with a variation to the traditional isoconversion method. The isoconversion method considers the time to achieve a particular conversion (or the rate of change of conversion if using the differential method), as their independent variable for then determining the activation energy.

Whilst the isoconversion method is suitable (and equivalent to the isomass method) for Fe_2O_3 , the isoconversion is not suitable (and not equivalent to the isomass method) for the perovskites with an undetermined initial non-stoichiometry. The perovskites starting non-stoichiometry ($3-\delta$) of O is unknown, therefore m_i cannot be defined. The OCs in this project are not entirely reduced so the final mass is also unknown, therefore m_f cannot be defined. Consequently, the conversion degree from full oxidation to entirely reduced for the perovskites cannot be defined. An alternative is the isomass method, which considers the relative mass loss (defined by equation 12). An advantage of using isomass/isoconversion method is that knowledge of the specific kinetic model used to represent the mass loss behaviour does not have to be defined, which is particularly useful when working with reactions with difficult to describe behaviours (e.g. 2 phase oxygen release mechanisms during reduction).

For each OC material, 4 redox cycles were completed at each isotherm, yet only the final reduction cycle will be used to fit the data. This is because the final curve often reaches a steady state cyclic behaviour, which is of key interest. Steady state cyclic behaviour of an oxygen carrier has been achieved when the relative mass loss (m_r) at time t, for cycle i, is equivalent to the relative mass loss at time t, for cycle $i+1$ (rel mass loss_{cycle i}^(t) = rel mass loss_{cycle $i+1$} ^(t)) hence each redox cycle beyond the 4th cycle is assumed to equal the same relative mass loss as to that of the 4th reduction cycle.

The isomass method derivation starts by considering the rate of change of relative mass loss:

$$\frac{dm_r}{dt} = \frac{m^{(t)} - m^{(t+\Delta t)}}{m^{(t=0)}\Delta t} \quad (14)$$

Where, $\frac{dm_r}{dt}$ is the rate of change of relative mass loss (s^{-1}), $m^{(t)}$ is the mass at time t (g), $m^{(t+\Delta t)}$ is the mass at the next time step (g), $m^{(t=0)}$ is the mass at the start of the reaction (g), and Δt is the time step (s).

The isomass method considers the time taken for each reduction reaction to reach a

particular value of relative mass loss (t_{m_r}), which is represented by equation 15.

$$\int_0^{m_r} \frac{dm_r}{f(m_r)} = kC \int_0^{t_{m_r}} dt \quad (15)$$

$$t_{m_r} = \frac{F(m_r) - F(0)}{A \exp\left(-\frac{E_a}{RT}\right) C} \quad (16)$$

$$t_{m_r} = \frac{\exp\left(\frac{E_a}{RT}\right)}{A_a} \quad (17)$$

Where $A_a = \frac{AC}{F(m_r) - F(0)}$. With a log transformation the equation has a linear dependence, where the slope can be solved for, to extract E_a (equation 18).

$$\ln(t_{m_r}) = \frac{E_a}{RT} - \ln(A_a) \quad (18)$$

From this, the activation energy can be plotted as a function of relative mass loss. This is particularly useful when analysing the O₂ release behaviours of the OCs.

Isomass method limitations:

1. No specific function for the relative mass loss $f(m_r)$ has been defined. $f(m_r)$ is defined within A_a along with the pre-exponential factor A , as a result, the pre-exponential factor is unknown and therefore so is the specific rate constant. A_a can be extracted though, which equates to $\frac{AC}{F(m_r) - F(0)}$.
2. When using equation 18, at least 2 data points are required to calculate E_a for a target relative mass loss value. The isotherms of 300°C and 400°C are not likely to achieve any significant depth of reduction. Consequently, the data points from the 500°C and 600°C isotherm are used to calculate E_a at a target relative mass loss. The depth of reduction achieved by the 600°C isotherm is expected to be greater than the depth of reduction achieved by the 500°C isotherm within the 2400 second reduction period. Consequently, the activation energy can only be considered up to the maximum depth of reduction achieved by the 500°C isotherm, beyond this there is only 1 data point from the 600°C isotherm, which is insufficient to calculate the key characteristics of the linear equation 18.

To quantify the limiting factor of the pellets during a reaction (either reaction rate or diffusion rate limited), the thiele modulus has been employed, which is defined by:

$$\phi = R_p \sqrt{\frac{k_v}{D_{eff}}} \quad (19)$$

Where ϕ is the thiele modulus, R_p is the pellet radius (m), k_v is the rate constant (s^{-1}), D_{eff} is the effective diffusivity ($\frac{m^2}{s}$).

D_{eff} is calculated from the molecular diffusivity (D_{mol}). D_{mol} for H₂ 5% in N₂ can be calculated for specific operating conditions of a given T (K) and P (atm) through the Fuller, Schettler, and Giddings equation 20 [22]:

$$D_{mol} = \frac{10^{-3}T^{1.75} \left(\frac{1}{M_A} + \frac{1}{M_B} \right)^{0.5}}{P \left(\left((\sum V_A)^{\frac{1}{3}} + (\sum V_B)^{\frac{1}{3}} \right) \right)^2} \quad (20)$$

D_{mol} is the molecular diffusivity (m²/s), M_A and M_B is the molecular weight of species A and B respectively. $\sum V_A$ and $\sum V_B$ are the sums of the diffusion volumes for species A and B respectively.

D_{eff} for a pellet of particular interest can be calculated from the D_{mol} with the following equation:

$$D_{eff} = \frac{\epsilon}{\tau} D_{mol} \quad (21)$$

The porosity (ϵ) for the pellets are stated in Table 4. D_{mol} is defined above by equation 20. The tortusity (τ) of a pellet is directly linked to the porosity, and is calculated using the Prieur, Plessis and Masliyah [23] equation for a consolidated, granular pellet:

$$\tau = (1 - (1 - \epsilon)^{2/3})\epsilon \quad (22)$$

As the solid-gas OC reaction takes place, the volumetric rate is not constant as the rate of O₂ decoupling from the OC is not linear with time. The volumetric rate can be calculated from the following equation:

$$k_v = \frac{r_{measure}}{V_p \eta(\phi) C} \quad (23)$$

Where $r_{measure}$ is the rate of O₂ decoupling ($\frac{mol_{O_2}}{s}$), V_p is the volume of the pellet (m³), and η is the effectiveness factor which is a function of ϕ . Whilst equations for $\eta(\phi)$ vary based on the geometry of the pellet, this project assumes $\eta=1$. $\eta=1$ assumes that the

reactant diffuses quickly throughout the pellet [24]. This assumption will be validated if the thiele modulus is found to be small. C is the concentration of the H₂ reducing agent, calculated to be: $C_{T=300^\circ C} = 0.355 \frac{mol}{m^3}$, $C_{T=400^\circ C} = 0.302 \frac{mol}{m^3}$, $C_{T=500^\circ C} = 0.263 \frac{mol}{m^3}$, and $C_{T=600^\circ C} = 0.232 \frac{mol}{m^3}$.

As the $r_{measure}$ changes with time and consequently k_v , a generalisation for a particular point in time can be made for the reaction rate and thiele modulus through equations 24 and 25:

$$k_v^{(t)} = \frac{r_{measure}^{(t)}}{V_p \eta_C} \quad (24)$$

Continuing the time generalisation to ϕ gives:

$$\phi^{(t)} = R \sqrt{\frac{k_v^{(t)}}{D_{eff}}} \quad (25)$$

From this, ϕ can be represented as a function of time, during the reduction reaction.

3.4 Scanning Electron Microscope

Scanning Electron Microscope (SEM) (Thermo Fisher Scientific - Phenom SEM) was used to investigate pellet porosity and was used to check if KOH had reached the core of the pellets for SrFeO_{3- δ} , LaFeO_{3- δ} and 1LaFeO_{3- δ} :9Fe₂O₃ through the process of Energy Dispersive Spectrometry (EDS), and performing regional scans within the pellet cores. The pellet cores were exposed through a simple cracking procedure.

3.5 Packed Bed Reactor

3.5.1 Reactor Set Up, Gas Injection Schedule, Exhaust Analysis

A fixed packed bed reactor (PBR) was used to investigate the CLHP material at scale (113.19g of 1LaFeO_{3- δ} :9Fe₂O₃ OC pellets) with Figure 8 showing a schematic of the reactor setup. Heating was achieved by electrical heating elements rated to 550°C. The heating element temperatures were controlled at $\sim 490^\circ C$, whilst the bed temperature was monitored. The operating pressure was P=1atm. A k-type thermocouple was installed at the top of the reactor for temperature monitoring within the bed. The gas flows were controlled by 3 Bronkorst EL-FLOW select F-201CV Mass Flow Controllers (MFC). The

OC materials filled from the base of the reactor bed, leaving the top section of the bed reactor empty. The exhaust gas was channelled through a condenser and through a CaCl_2 desiccant before being analysed using the ABB EL3020 for CO_2 , CO and $\text{H}_2:\text{N}_2$ analysis.

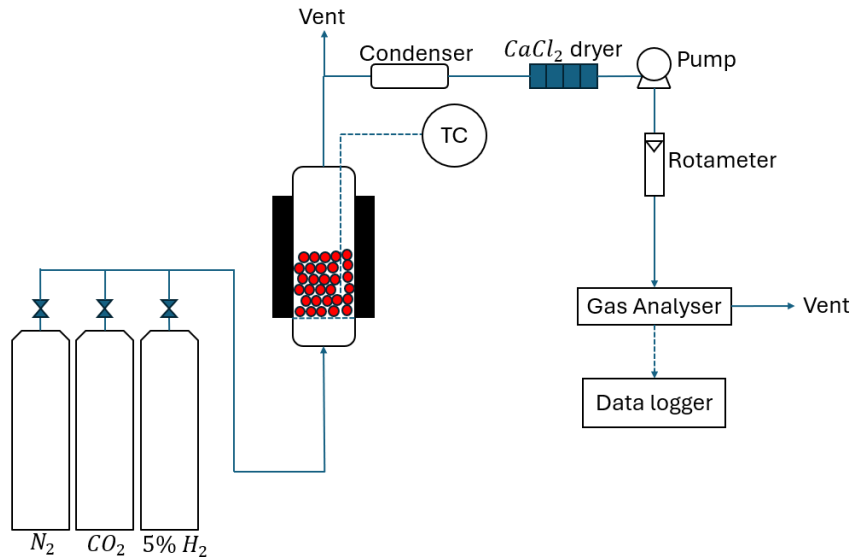


Figure 8: PBR Schematic for the H_2 production prototype.

The 3 MFCs had to be calibrated for accurate use, and the CO MFC was used for CO_2 flow in this project, and hence had to be re-tuned (for detailed information on the MFC calibration using a gilibrator, check Appendices Section A).

A cyclic RWGS experiment was carried out first at NTP, to test the zero and span levels of the ABB EL3020 gas analyser.

The sequence of gas streams used, along with their flow rates and duration are shown in Table 5.

Table 5: Gas Stream Sequence for PBR Operation

Gas	Flow Rate (lN/min)	Duration (seconds)
N_2^1	2	50
H_2 (5%) ²	2	240
N_2^1	2	100
CO_2^3	2	240
N_2^1	2	100
H_2 (5%) ²	2	900
N_2^1	2	100
CO_2^3	2	900
N_2^1	2	100

¹ Purge Gas.

² Reducing Gas.

³ Oxidising Gas.

4. Results

4.1 Phase Identification

4.1.1 $\text{La}_{0.5}\text{Sr}_{0.5}\text{FeO}_{3-\delta}$

For the $\text{La}_{0.5}\text{Sr}_{0.5}\text{FeO}_{3-\delta}$ sample (XRD sample with the rietveld refined plot is shown in Figure 9) there is difficulty highlighting which phase is present throughout the refinement process. At first, $\text{La}_{0.5}\text{Sr}_{0.5}\text{FeO}_{3-\delta}$ (ICSD 674775) matches the scattering peaks, however, by mixing the stoichiometric precursors $\text{La}_2(\text{CO}_3)_3$, SrCO_3 and Fe_2O_3 through a solid state synthesis preparation method, is it possible to produce the perovskites $\text{LaFeO}_{3-\delta}$ and $\text{SrFeO}_{3-\delta}$ as well, as they can all be synthesised from the same precursors. Figures 10 (a) and (b) are plots of 2 specific peaks, both which have a shoulder peak present. The XRD apparatus has a monochromator resulting in just $\text{Cu-K}_{\alpha 1}$ radiation present, hence there are no shoulder peaks from $\text{Cu-K}_{\alpha 2}$ radiation. The leftmost peaks are related to the $\text{LaFeO}_{3-\delta}$ perovskite, and the rightmost peaks are related to $\text{La}_{0.5}\text{Sr}_{0.5}\text{FeO}_{3-\delta}$ and/or $\text{SrFeO}_{3-\delta}$. The solid state synthesis procedure discussed in the Material Preparation for perovskites is not suitable for producing phase pure $\text{La}_{0.5}\text{Sr}_{0.5}\text{FeO}_{3-\delta}$ samples, as it will likely produce alternative perovskites including; $\text{LaFeO}_{3-\delta}$ and $\text{SrFeO}_{3-\delta}$.

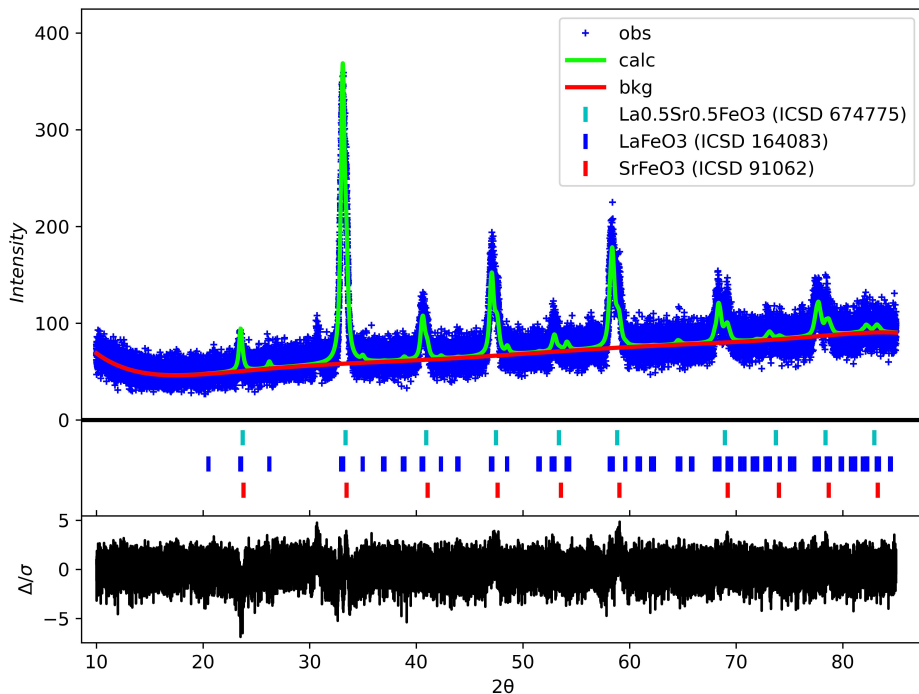


Figure 9: XRD scan and rietveld refinement of $\text{La}_{0.5}\text{Sr}_{0.5}\text{FeO}_{3-\delta}$ sample.

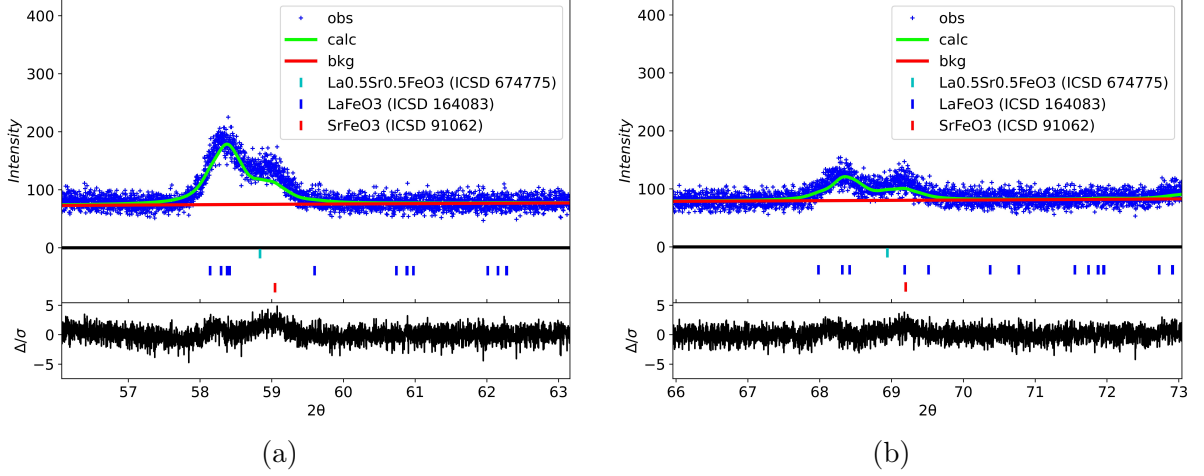


Figure 10: (a) Zoomed peak inspection of the potential $\text{La}_{0.5}\text{Sr}_{0.5}\text{FeO}_{3-\delta}$ sample for $2\theta \in [56.0, 63.1]^\circ$. (b) Zoomed peak inspection of the potential $\text{La}_{0.5}\text{Sr}_{0.5}\text{FeO}_{3-\delta}$ sample for $2\theta \in [66.0, 73.0]^\circ$.

4.1.2 $\text{LaFeO}_{3-\delta}$

Figure 11 shows the XRD and rietveld refinement for the $\text{LaFeO}_{3-\delta}$ perovskite. The ICSD 164083 resulted in a good fit, hence solid state synthesis is suitable for the production of $\text{LaFeO}_{3-\delta}$ perovskites.

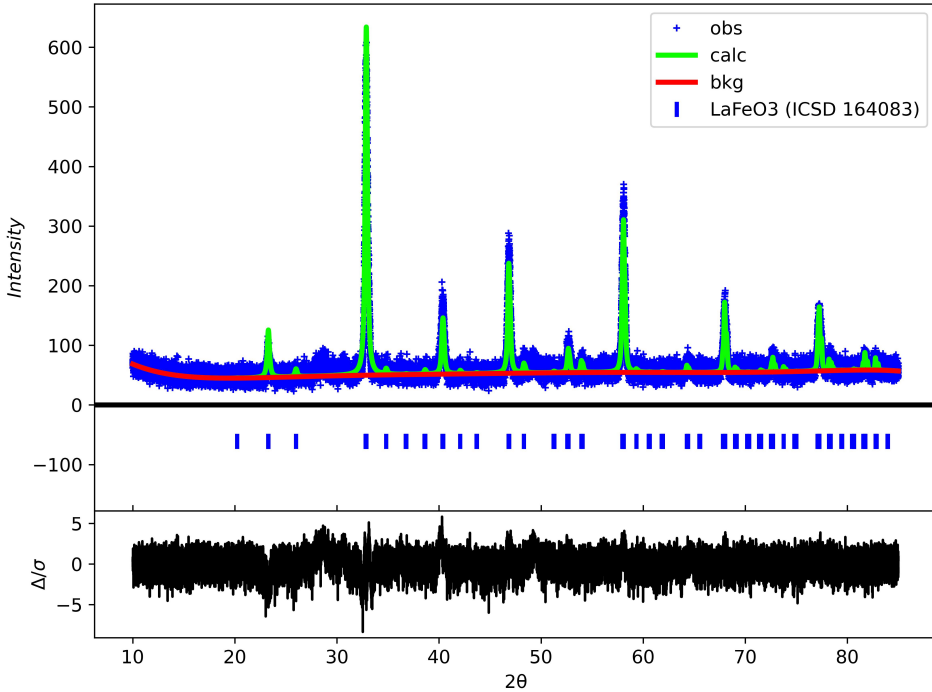


Figure 11: XRD scan and Rietveld refinement of the $\text{LaFeO}_{3-\delta}$ sample.

4.1.3 SrFeO_{3- δ}

Figure 12 shows the XRD and Rietveld refinement for the SrFeO_{3- δ} perovskite. The ICSD 91062 resulted in a good fit, hence solid state synthesis is suitable for the production of SrFeO_{3- δ} .

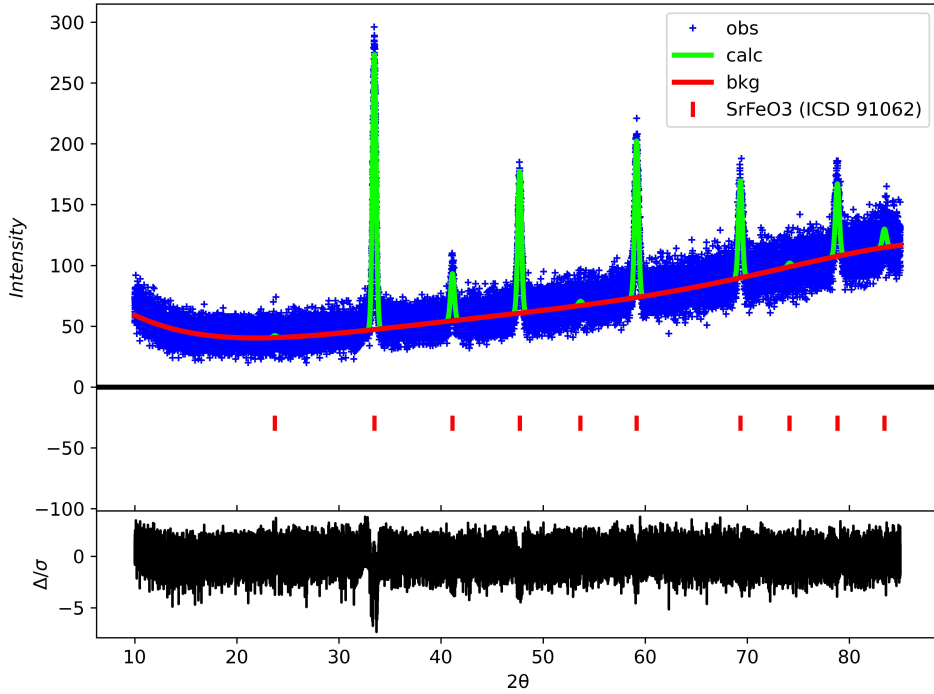


Figure 12: XRD scan and Rietveld refinement of the SrFeO_{3- δ} sample.

4.1.4 KOH Doped Oxygen Carriers

The effect of KOH impregnation was also investigated through XRD material characterisation. With the KOH impregnation method, the KOH doping could result in an entirely new phase (new scattering peaks present) representing the KOH crystals, or the K⁺ ions could have diffused into the crystal structure of the perovskites itself, which would be represented by a peak shift. Diffusion into the crystal structure will effect the XRD scattering angles by a small peak shift or possible peak broadening [25]. When doping with a material, an increase in ionic radius will result in a negative peak shift (scattering peaks shift to a smaller scattering angle), in contrast a decrease in ionic radius will result in a positive peak shift (scattering peaks shift to a greater scattering angle) [25]. This inverse relation can also be proven by the Bragg's Law - equation 6.

Whilst Figure 12 displays the XRD pattern of the SrFeO_{3- δ} , understanding the effects of KOH doping can be completed through the analysis of individual scattering peaks. Figure 13 shows individual scattering peak comparisons for SrFeO_{3- δ} vs 10wt% KOH/SrFeO_{3- δ} , located within $2\theta \in [33.0, 34.2]^\circ$ and $2\theta \in [58.6, 60.2]^\circ$ ranges respectively. Figure 14

shows individual scattering peak comparisons for $\text{LaFeO}_{3-\delta}$ vs 10wt% KOH/ $\text{LaFeO}_{3-\delta}$, located within $2\theta \in [32.3, 33.5]^\circ$ and $2\theta \in [57.6, 58.7]^\circ$ ranges respectively. Figure 15 shows individual scattering peak comparisons for $1\text{LaFeO}_{3-\delta}:9\text{Fe}_2\text{O}_3$ and 10wt% KOH/Sr $\text{FeO}_{3-\delta}$, located within $2\theta \in [33.5, 34.4]^\circ$ and $2\theta \in [36.0, 37.2]^\circ$ ranges respectively. All KOH impregnated samples have a positive peak shift in their scattering angles. This is unexpected, due to K^+ ions having an ionic radius of 1.37\AA (coordination IV), which is greater than the ionic radii for Sr^{2+} (1.18\AA , coordination IV), La^{+3} (1.032\AA , coordination IV), Fe^{2+} (0.63\AA , coordination IV), and Fe^{3+} (0.49\AA , coordination IV) [26]. The larger K^+ ions should have resulted in a negative peak shift due to the planar spacing's increasing and the scattering angle decreasing as a result. Interstitial substitution may be disregarded as the dopant K^+ ions are not sufficiently small to diffuse into the interstices of the crystal [27]. Interstitial substitution is more common from the p-block elements with smaller radii [27]. Whilst the KOH impregnation did not result in any new scattering peaks for any of the samples, peak shift was present, yet in the unexpected direction. K was detected within the cores of the impregnated pellet samples from a regional scan, using SEM, and with no additional peaks present, K may be within the crystal structure or be present as an amorphous phase (Figure 16 shows the Secondary Electron Detector scans for 10wt% KOH/Sr $\text{FeO}_{3-\delta}$ (a), 10wt% KOH/ $\text{LaFeO}_{3-\delta}$ (b), and 10wt% $1\text{LaFeO}_{3-\delta}:9\text{Fe}_2\text{O}_3$ (c)). With a target of 10wt% KOH, this relative amount may not be sensitive enough to detect through XRD. This unexpected observation in peak shift can be explained as the KOH doped samples were originally pelletised before impregnation, whilst the undoped samples remained as powders during their XRD scans. As a result of pelletisation, compressive stresses will have been induced onto the crystal structures. The compressive stresses from the pelletisation may have influenced the 10wt% KOH doped samples, resulting in an decreased planar spacing, and from Bragg's Law this corresponds to a positive peak shift, as seen in Figures 13, 14, and 15. Only macro-strain is identified due to peak shifts present, micro-strain corresponding to peak broadening is not present in the scan [28]. Whilst the pellets were fired at 1000°C , Götsch et al. [14] shows that heating will temporarily, negatively shift the scattering peaks as a result of thermal expansion of the planar spacing, and upon cooling, they will return to their original crystal structure (Figure 3).

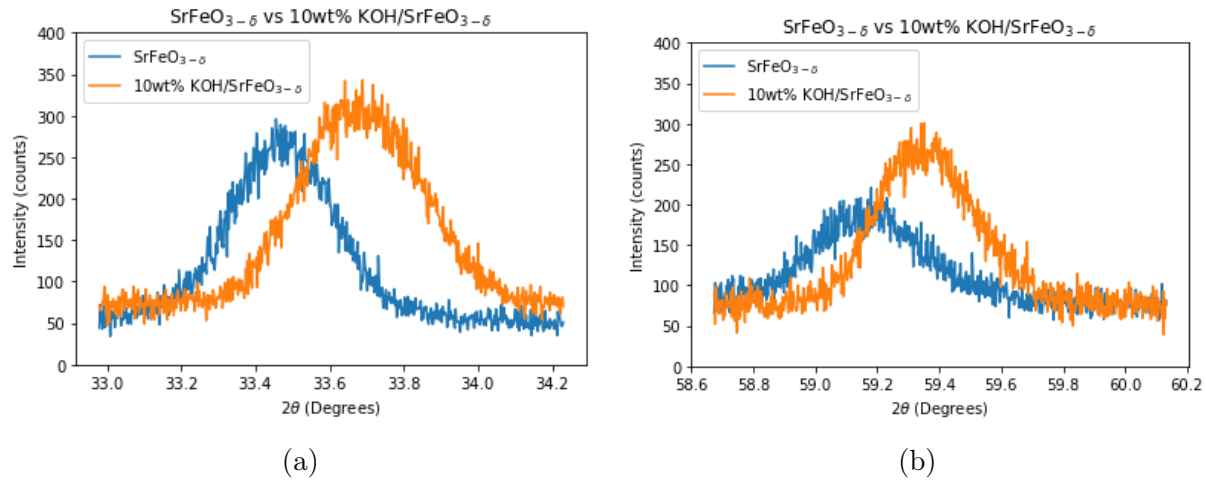


Figure 13: (a) XRD zoomed peak comparison between $\text{SrFeO}_{3-\delta}$ and 10wt% KOH/ $\text{SrFeO}_{3-\delta}$ within the range $2\theta \in [33.0, 34.2]^\circ$. (b) XRD zoomed peak comparison between $\text{SrFeO}_{3-\delta}$ and 10wt% KOH/ $\text{SrFeO}_{3-\delta}$ within the range $2\theta \in [58.6, 60.2]^\circ$.

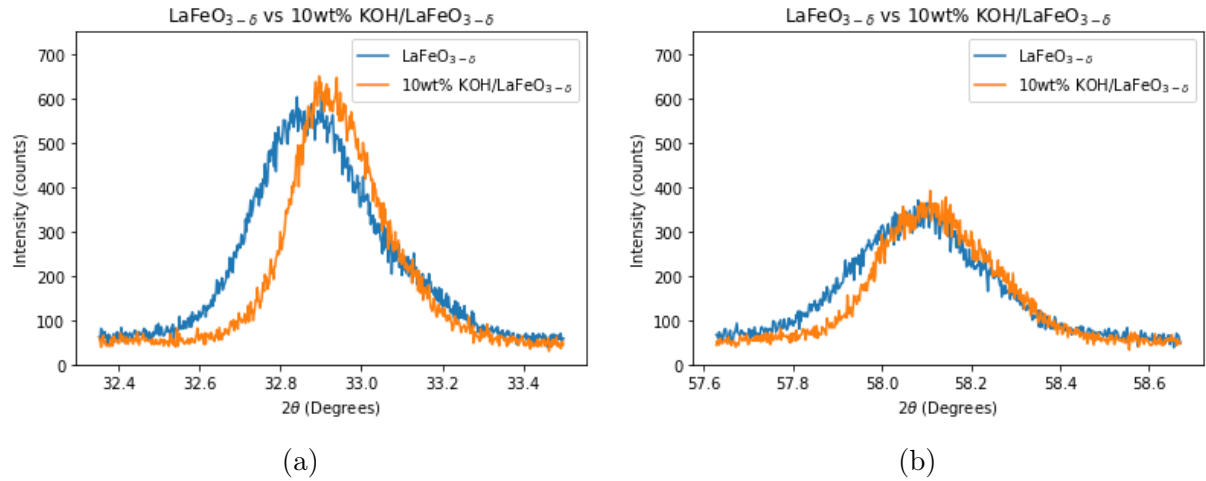


Figure 14: (a) XRD zoomed peak comparison between $\text{LaFeO}_{3-\delta}$ and 10wt% KOH/ $\text{LaFeO}_{3-\delta}$ within the range $2\theta \in [32.3, 33.5]^\circ$. (b) XRD zoomed peak comparison between $\text{LaFeO}_{3-\delta}$ and 10wt% KOH/ $\text{LaFeO}_{3-\delta}$ within the range $2\theta \in [57.6, 58.7]^\circ$.

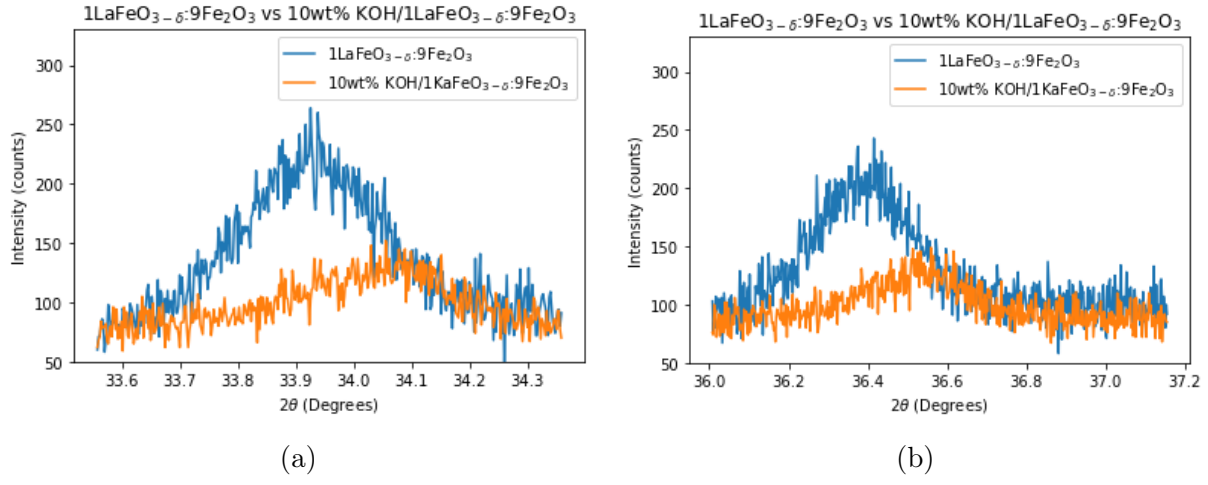


Figure 15: (a) XRD zoomed peak comparison between $1\text{LaFeO}_{3-\delta}\text{:9Fe}_2\text{O}_3$ and $10\text{wt\% KOH}/1\text{LaFeO}_{3-\delta}\text{:9Fe}_2\text{O}_3$ within the range $2\theta \in [33.5, 34.4]^\circ$. (b) XRD zoomed peak comparison between $\text{LaFeO}_{3-\delta}$ and $10\text{wt\% KOH}/\text{LaFeO}_{3-\delta}$ within the range $2\theta \in [36.0, 37.2]^\circ$.

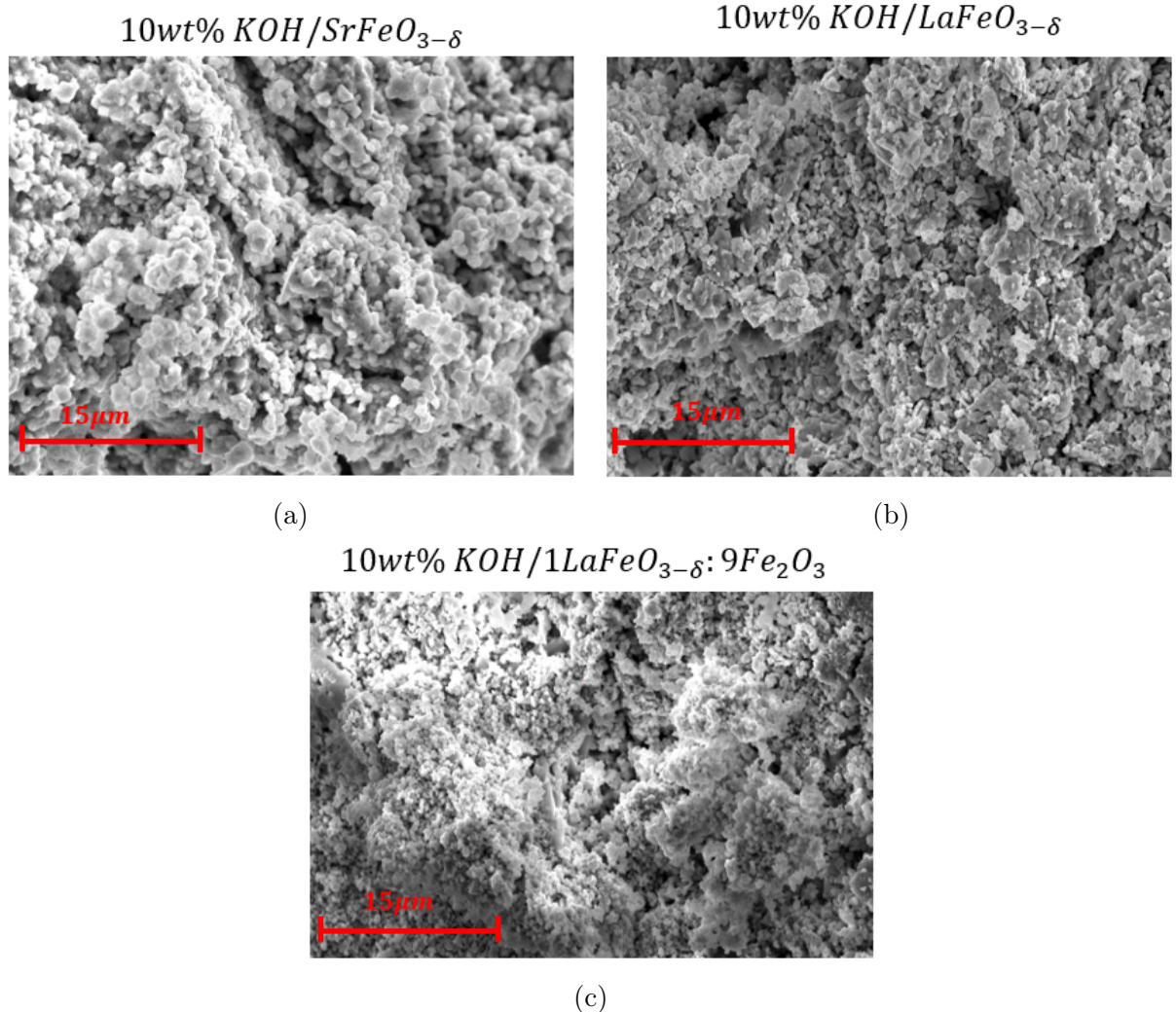


Figure 16: SEM scans for $10\text{wt\% KOH}/\text{SrFeO}_{3-\delta}$, $10\text{wt\% KOH}/\text{LaFeO}_{3-\delta}$, and $10\text{wt\% KOH}/1\text{LaFeO}_{3-\delta}\text{:9Fe}_2\text{O}_3$ as (a), (b), and (c) respectively.

4.2 TGA Results

4.2.1 Fe₂O₃ Pellet vs Fe₂O₃ Powder

The H₂ producing capability and redox stability of pelletised and powdered Fe₂O₃ samples were investigated at 300°C, 400°C, 500°C and 600°C (4 redox cycles per isotherm). The TGA relative mass change results are shown in Figure 17, with (a) displaying the pellet sample results and (b) displaying the powder sample results.

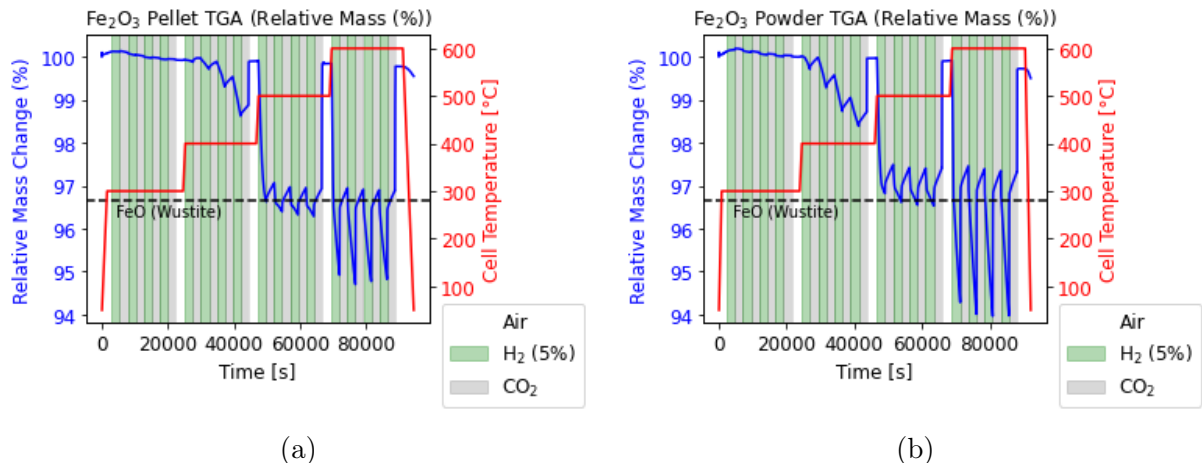


Figure 17: TGA cycles for the Fe₂O₃ Pellet sample (a) and Powder sample (b).

In Figure 17 (a) and (b) the 400°C isotherm does not reach a steady cyclic redox behaviour, as it is seen to drift downwards with each successive cycle. This can also be seen by analysing the individual relative mass loss curves at the 400°C isotherm, shown in Figure 18 below, where each of the curves achieve a differing depth of reduction. This is a result of the Fe₂O₃ samples reducing to a H₂ producing phase (where FeO is present). If more than 4 cycles were tested at the 400°C isotherm, it is expected that the redox behaviour would eventually reach a repeatable, steady state process. Steady state redox behaviour can be seen when the relative mass change for each successive cycle follows the same trend as the previous cycle (this behaviour can be seen from the relative mass changes at the 500°C and 600°C isotherm), this repeatable pattern is possible when the oxidisation cycle is also repeatable, hence reaching a steady state cyclic behaviour.

Assuming that the pellet and powdered samples of Fe₂O₃ are reducing homogeneously throughout, a label has been plotted on Figure 17 (a) and (b), highlighting the relative mass loss where FeO would start to form (96.667wt%). FeO has a significantly greater oxidation ability in CO₂ in contrast to Fe₃O₄, at 400°C. From Figure 17 (a) and (b), the samples oxidise (increase in relative mass) at the 400°C isotherm, in a CO₂ oxidising environment. The significant factor here, is the size of the relative mass gain occurring before the FeO phase has been homogeneously achieved. At 400°C, the partial pressure of

O_2 in equilibrium with Fe_3O_3 and Fe_2O_3 is $pO_2 = 10^{-23} \text{ atm}$. Upon Fe_3O_4 oxidising and reaching an equilibrium with Fe_2O_3 , this would correspond to a minimal mass gain in the presence of the CO_2 oxidising agent, with $\frac{P_{CO}}{P_{CO_2}} = 7.5 \times 10^{-5}$. To allow for the large relative mass increase during the CO_2 oxidation at 400°C , a deeper phase of iron oxide must be present. This also proves that the original assumption of the pellet and powdered samples reducing homogeneously is false.

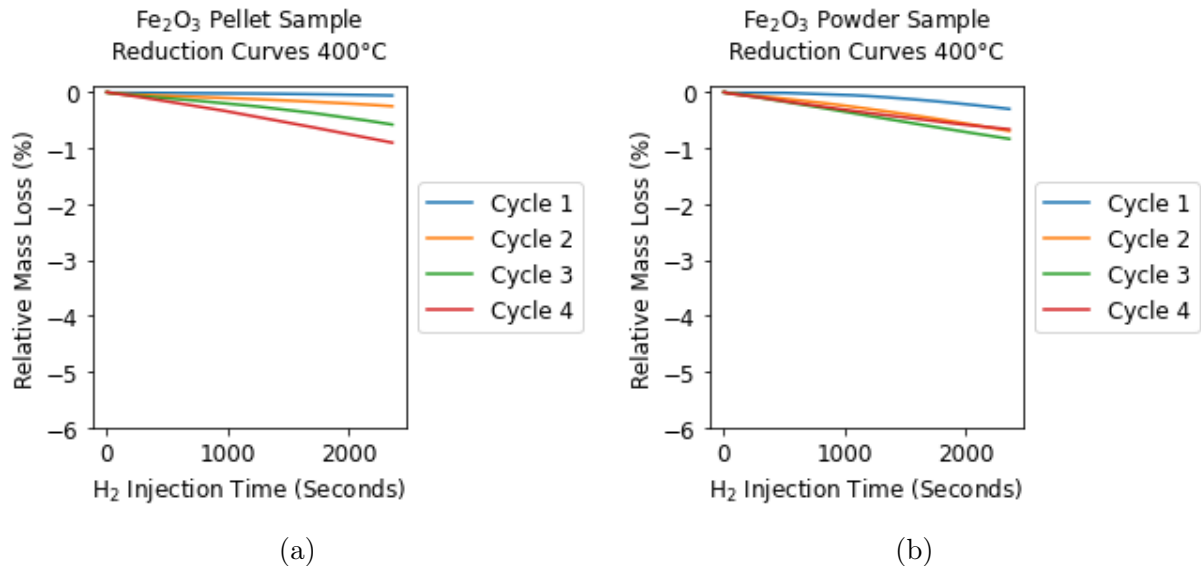


Figure 18: 400°C isothermal reduction relative mass losses for (a) Fe_2O_3 Pellet and (b) Fe_2O_3 Powder.

As for the 500°C and 600°C isotherms, a steady state cyclic redox has been achieved in both the pellet and the powder samples. This is shown in Figure 17 (a) and (b) at the 500°C and 600°C isotherm, where the redox cycles do not drift overall, and have a minimal net relative mass change, per redox cycle. This steady state cyclic behaviour can also be seen through the relative mass loss curves in Figure 19 (500°C) and Figure 20 (600°C), where each successive reduction curve follows the same behaviour as the previous cycle. 'Cycle 1' has a different reduction behaviour at 500°C and 600°C because it is decoupling from O_2 so it can reach a suitable H_2 producing phase. Whilst the pellet and powder samples of Fe_2O_3 have reached a steady state redox phase, they were only tested for 4 redox cycles. Iron oxide being used as an OC in CL is known to experience sintering and agglomeration after several redox cycles [5, 16, 17]. Therefore, if more than 4 redox cycles were completed, what would be expected on Figures 19 and 20, is that the magnitude of relative mass loss achieved per reduction cycle, will degrade and reduce.

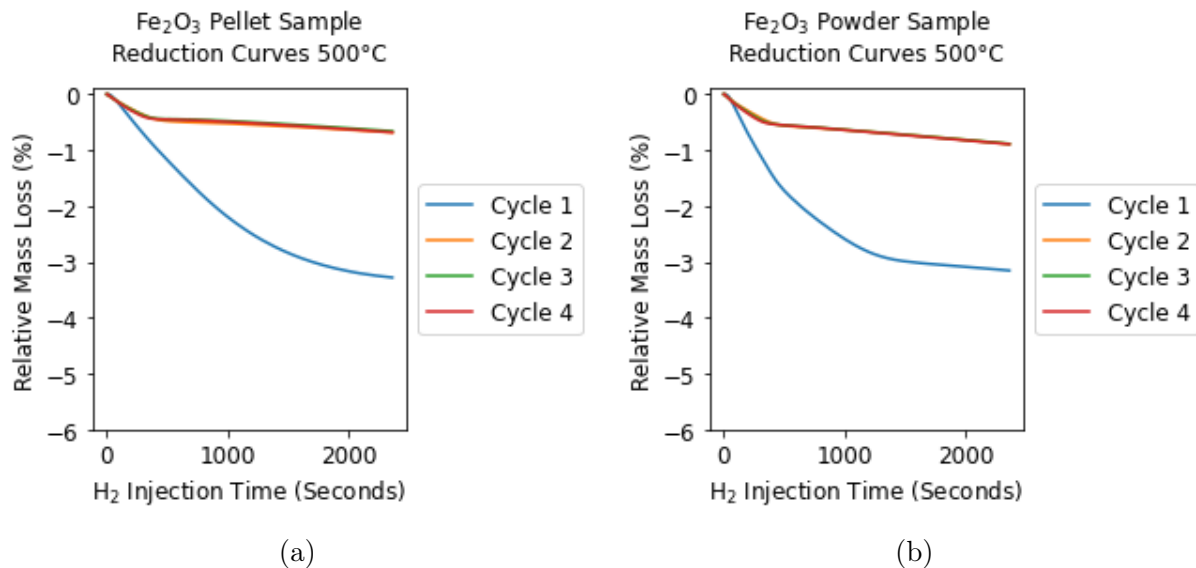


Figure 19: 500°C isothermal reduction relative mass losses for (a) Fe₂O₃ Pellet and (b) Fe₂O₃ Powder.

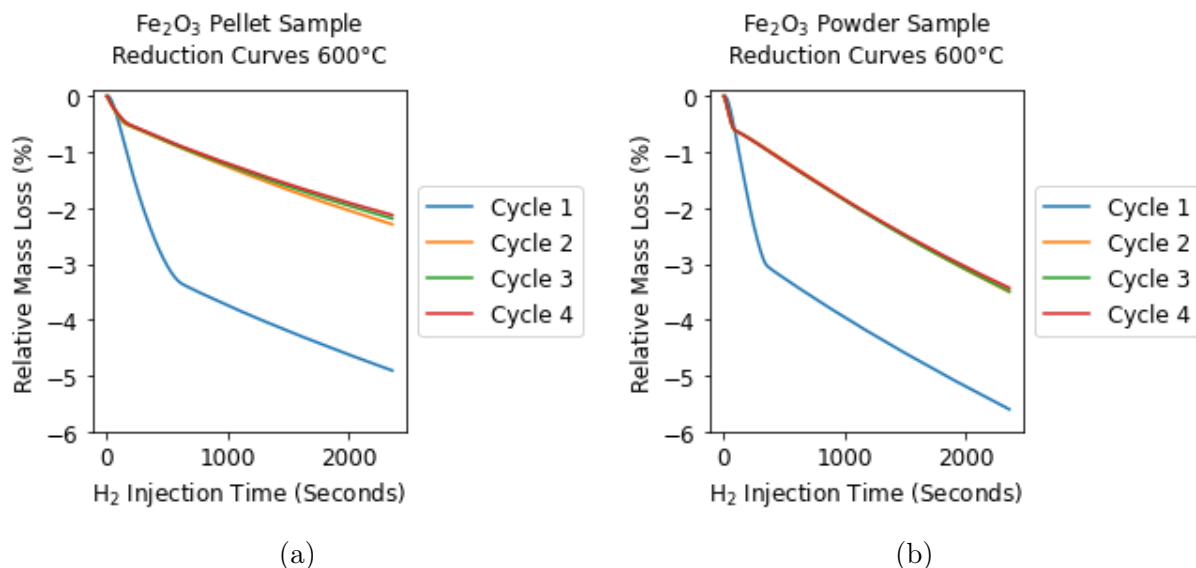


Figure 20: 600°C isothermal reduction relative mass losses for (a) Fe₂O₃ Pellet and (b) Fe₂O₃ Powder.

Upon reaching a steady state cyclic redox behaviour, at 500°C the reduction mass loss curves for both the pellet (Figure 19 (a)) and the powder (Figure 19 (b)) follow a very similar trend. Therefore, the reduction reaction is slow enough that gas diffusion through the pellet is not limiting. However, what must be considered is that the Fe₂O₃ powder sample, when loaded into the alumina crucible for the TGA experiment, could form a pellet like structure where only the top surface experiences a reduction, replicating a pellet like behaviour.

The thiele moduli of the pellet also confirms that gas diffusion is not limiting, due to the very low magnitude (the thiele moduli for each isotherm at the start and end of

the reduction cycle is shown in Table 6). The methodology assumes an effectiveness factor (η) to be 1 (not gas diffusion limited), and with the thiele moduli magnitudes being significantly small, the assumption of $\eta=1$ is strong. At 400°C the thiele modulus actually increases, in contrast to an expected decrease, this is possibly due to the unstable cyclic behaviour of the Fe₂O₃ sample at 400°C, whilst it is still reducing until it reaches a consistent H₂ producing phase.

Table 6: Fe₂O₃ pellet thiele moduli at the start of the reduction cycle (t=0s) and at the end of the reduction cycle (t=2400s) for the 400°C, 500°C and 600°C isotherms.

Fe ₂ O ₃ Pellet	t=0s	t=2400s
400°C	2.1×10^{-5}	2.4×10^{-5}
500°C	3.4×10^{-5}	1.2×10^{-5}
600°C	5.6×10^{-5}	2.2×10^{-5}

The temperature dependent molecular diffusivities for 1.67% H₂ in N₂ were calculated to be: $D_{\text{mol},400^\circ\text{C}} = 3.15 \times 10^{-4} \frac{\text{m}^2}{\text{s}}$, $D_{\text{mol},500^\circ\text{C}} = 4.02 \times 10^{-4} \frac{\text{m}^2}{\text{s}}$, and $D_{\text{mol},600^\circ\text{C}} = 4.97 \times 10^{-4} \frac{\text{m}^2}{\text{s}}$. D_{eff} were dependent on the pellets porosities and tortuosity, highlighted in Table 4 and calculated using equation 21.

The small thiele modulus, and the behaviour of the pellet reduction curves being similar to the powder reduction curves, suggests that there is not gradient from the inside to the outside of the pellet caused by gas diffusion. Hence all the pores have an equivalent gas concentration. However, there is still an interesting 2 phase O₂ behaviour which is present at the 500°C isotherm (Figure 19) and 600°C isotherm (Figure 20) for both the pellet and the powder. The first phase of O₂ release finishes at $\sim 0.5\text{wt}\%$ relative mass loss for both the pellet and powder samples. Hence the 2 phase O₂ release mechanism is not unique to just the pellet, and is not a result of gas diffusion limitations. This 2 phase O₂ mechanism may be a consequence of the Fe₂O₃ particles not being sieved, and that particles of sizes $>355\mu\text{m}$ are likely to be present in the samples. The particles were not sieved as large pellets were to be produced, so minimal expectation of individual particles causing a significant behaviour was anticipated. Alternative literature when working solely with OC powders do sieve their particles [15, 29, 30]. With large grains present, and with a small pellet porosity=0.00114, there are large continuous domains of iron oxide present. This may result in the large individual grains converting in a step-wise fashion where only their outer layer is experiencing redox, so the local grains do experience a front, but the pellet does not. The particle sizes were found to play a key role in the depth of reduction achieved for Iron Oxide (on the μm scale) [29]. Particles between the sizes of 100 μm - 160 μm took approximately x4 longer to reduce in contrast to particles between the sizes of 1 μm - 1.5 μm [29]. Sieving the particles to smaller sizes e.g. 1 μm -1.5 μm may be necessary to improve the overall reactivity of the pellets. The actual improvement from using smaller particles can be related to porosity and surface area available of the particles.

Figure 21 displays the activation energy as a function of relative mass loss for the pellet and powder samples of Fe_2O_3 , where the activation energy has been solved for using the isomass method (discussed in Section 3.3). For both the pellet and the powder, there are 2 distinct activation energy levels present, with the powdered sample energy levels being less distinct. This supports the earlier identification that a 2 phase O_2 release mechanism is taking place. The transition between the 2 activation energy levels occurs at a relative mass loss of $\sim 0.45\text{-}0.50\text{wt\%}$, directly corresponding to the point for which the 2nd phase of O_2 release begins, shown in Figures 19 and 20. The instability present for the activation energy vs relative mass loss in Figure 21 is a result of a lack of data at alternative isotherms, as only the 500°C and 600°C isotherms resulted in insightful data related to the O_2 release behaviour. Additionally, this is commonly expected as a result of the integral method which is more susceptible to noise and anomaly data points, the differential method would have resulted in a smoother plot [31]. As a result, the instability has no significant meaning, other than a lack of isotherms were considered.

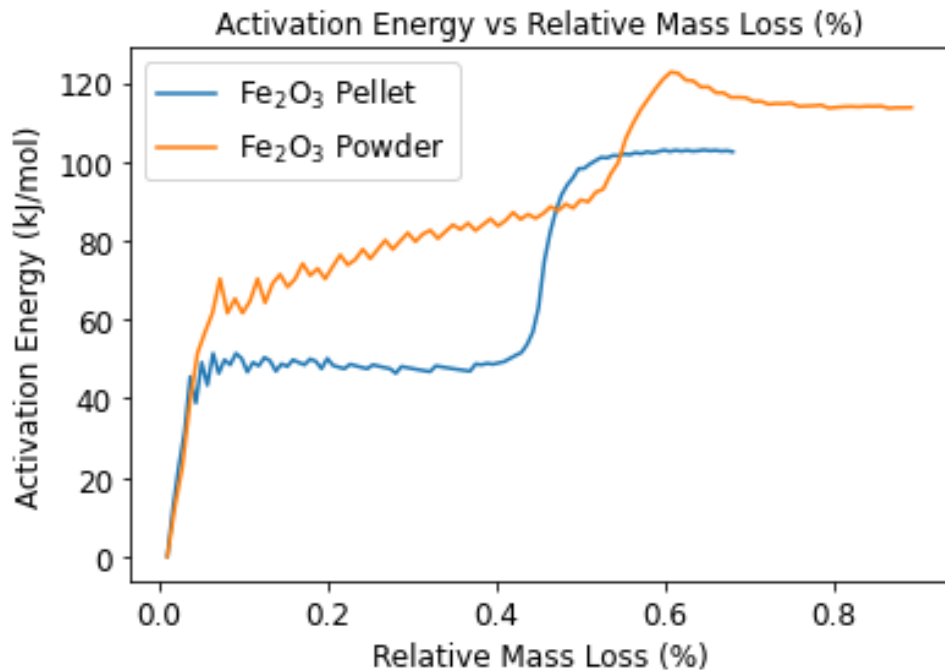


Figure 21: Activation Energy (kJ/mol) comparison of Fe_2O_3 pellet and Fe_2O_3 powder, as a function of relative mass loss (%).

4.2.2 SrFeO_{3-δ} Pellet vs 10 wt% KOH/SrFeO_{3-δ} Pellet

The H₂ producing capability and redox stability of SrFeO_{3-δ} and 10wt% KOH/SrFeO_{3-δ} pellet samples were investigated at 300°C, 400°C, 500°C and 600°C (4 redox cycles per isotherm). The TGA relative mass change results are shown in Figure 22, with (a) displaying the undoped KOH pellet results and (b) displaying the 10wt% KOH doped pellet results. Figure 22 (b) shows a sharp initial mass loss upon heating to 300°C, likely due to the evaporation of H₂O, and not due to O₂ decoupling in Air which has been identified to occur at ~400°C [15].

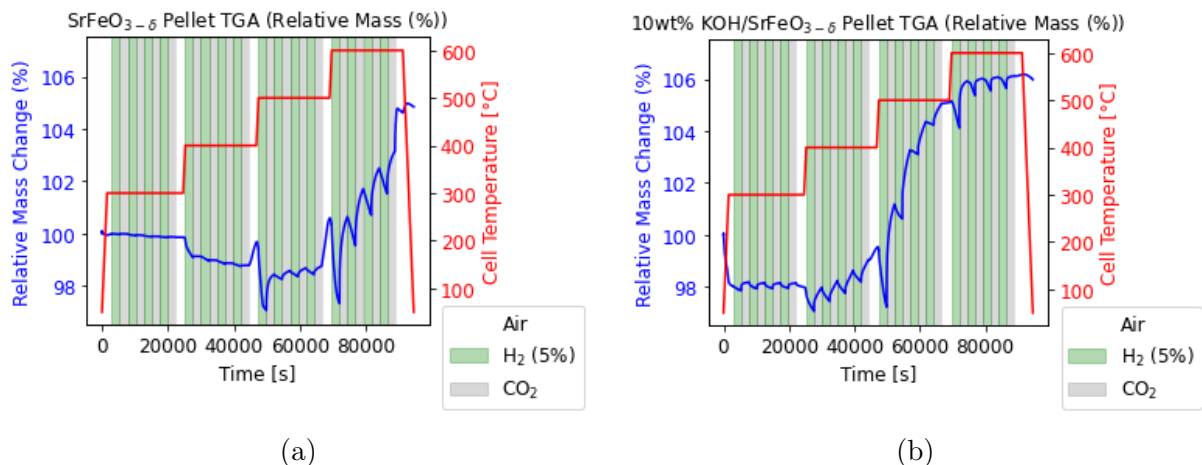


Figure 22: TGA cycles for (a) SrFeO_{3-δ} Pellet and (b) 10wt% KOH/SrFeO_{3-δ} Pellet.

When operating at the 300°C isotherm, there is minimal redox activity for the SrFeO_{3-δ} pellet (a), whilst the 10wt% KOH doped pellet does have a steady state cyclic behaviour, but with a small depth of reduction and oxidation being achieved.

As for the 400°C isotherm, the reduction curves (shown in Figure 23 below) show the undoped KOH pellet to be inactive and currently inert at this low temperature. Interestingly the 10wt% KOH doped pellet is showing signs of reactivity. But upon increasing the operating temperature to 500°C (Figure 24) the 10wt% KOH doped pellet behaviour changes, and becomes more inert and less reactive. Whilst the undoped KOH pellet starts to increase in reaction rate, as expected. From Figure 22 (b) at the 500°C isotherm, there is a significant mass gain occurring in CO₂, yet minimal mass loss occurring during H₂ reduction. This significant mass gain could be related to the KOH reacting with the CO₂ directly to form carbonates, and not improving the O₂ transfer kinetics. KOH has been considered before for CO₂ absorption in Carbon Capture and Storage (CCS), due to its ability to have a high uptake of CO₂ per gram of KOH [32, 33]. The carbonation reaction between KOH and CO₂ is given by:



With a 10wt% KOH doping content, this can result in an additional 5wt% relative mass increase just from KOH forming carbonates. Noticeably from Figure 22 (b) the pellet starts to gain mass at approximately 98wt%, and stabilises at 106wt%, this is greater than the 5wt% possible mass increase from a 10wt% KOH doping content. However, this additional relative mass increase could be related to the lack of control from wet impregnation. With additional KOH present beyond the 10wt% target, this could result in a greater than expected relative mass increase from KOH doping.

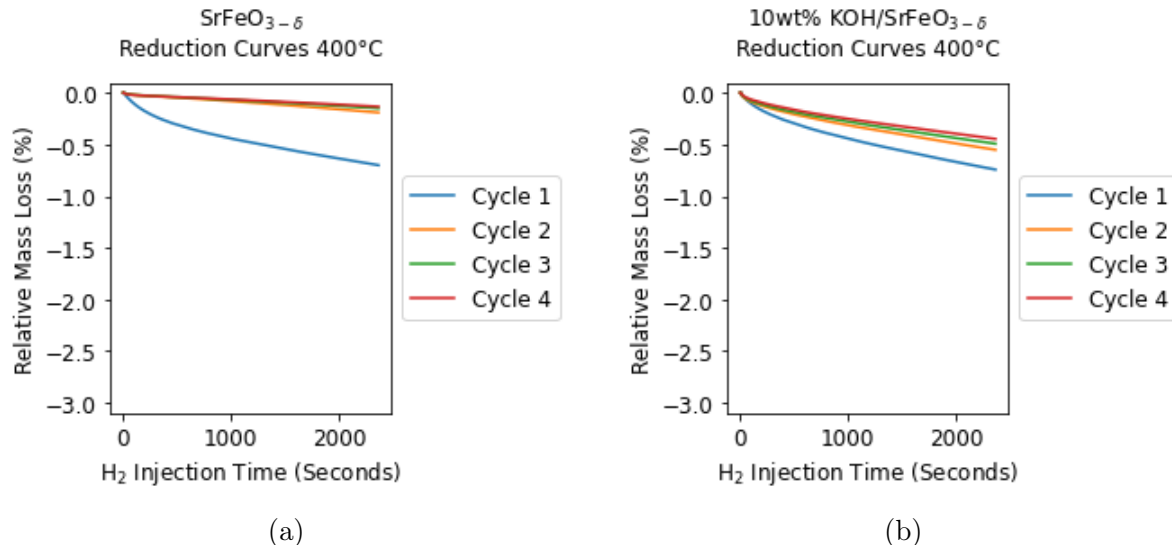


Figure 23: 400°C isotherm reduction relative mass loss curves for (a) $\text{SrFeO}_{3-\delta}$ (b) 10 wt% KOH/ $\text{SrFeO}_{3-\delta}$

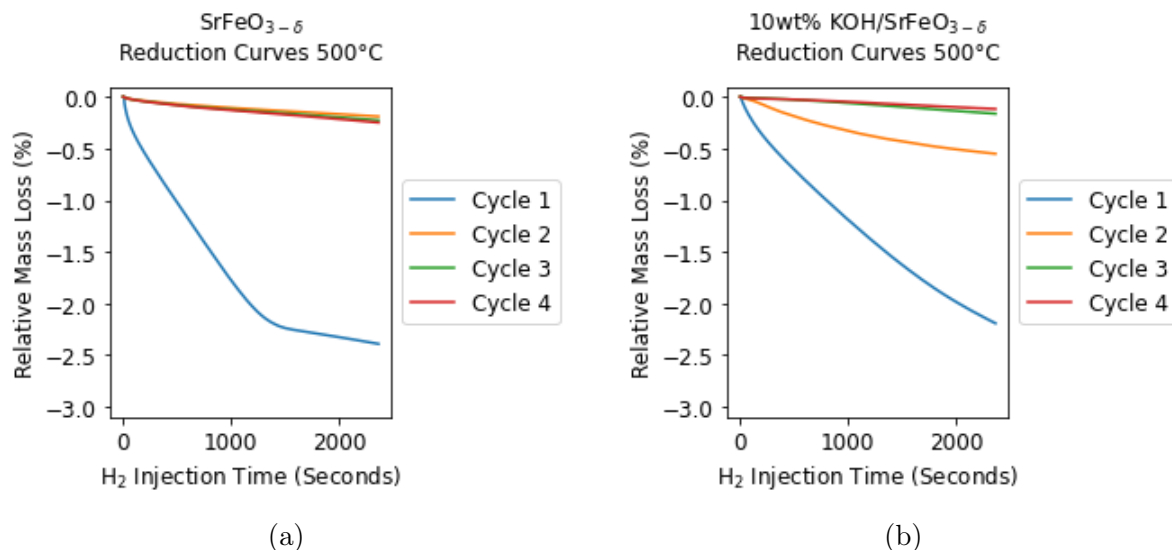


Figure 24: 500°C isotherm reduction relative mass loss curves for (a) $\text{SrFeO}_{3-\delta}$ (b) 10 wt% KOH/ $\text{SrFeO}_{3-\delta}$

Figure 25 shows the reduction mass loss curves for the undoped $\text{SrFeO}_{3-\delta}$ sample (a), and the 10wt% KOH/ $\text{SrFeO}_{3-\delta}$ sample (b) at the 600°C isotherm. The 10wt% KOH

doped pellet at 600°C experiences minimal reaction for the first 800 seconds (repeat experiments were completed to confirm this behaviour). With large relative mass gains being experienced at the 400°C, 500°C and 600°C isotherms of the KOH pellet (Figure 22 (b)) this can be from a large proportion of the 10wt% KOH fully reacting to form K₂CO₃ carbonates through reaction 26. Figure 22 (a) representing the undoped pellet does also experience a mass gain, but not as significant as the 10wt% KOH pellet (especially during the 500°C isotherm). As the relative mass increase begins to plateau for the 10wt% KOH pellet at the 600°C isotherm, this further supports the proposal that the 10wt% KOH has formed K₂CO₃, or that enough K₂CO₃ has formed to the point where it is inhibiting the redox reactions of the pellet. The inhibiting of the reaction could be the K₂CO₃ blocking the pores of the pellet, consequently effecting the gas diffusion within the pellet. Figure 25 shows the expected reduction curves for a pellet with an unblocked transport mechanism ((a) with 0wt% KOH), and the 10wt% KOH pellet (b) having significantly differing behaviours, this comparison further supports that the gas diffusion transport is likely blocked by the K₂CO₃ carbonates. Whilst this does not mean KOH is unsuitable for H₂ production, this should be further tested. However, for cyclic RWGS, the KOH is likely to inhibit the reaction mechanism, and is not recommended for use. Furthermore, this proposes a potential flaw with the use of cyclic RWGS to be used as a proxy for H₂ production, where the CO₂ oxidation phase may actively encourage the formation of carbonates. This results in misleading information about the true redox potential of the OC in a CLHP environment.

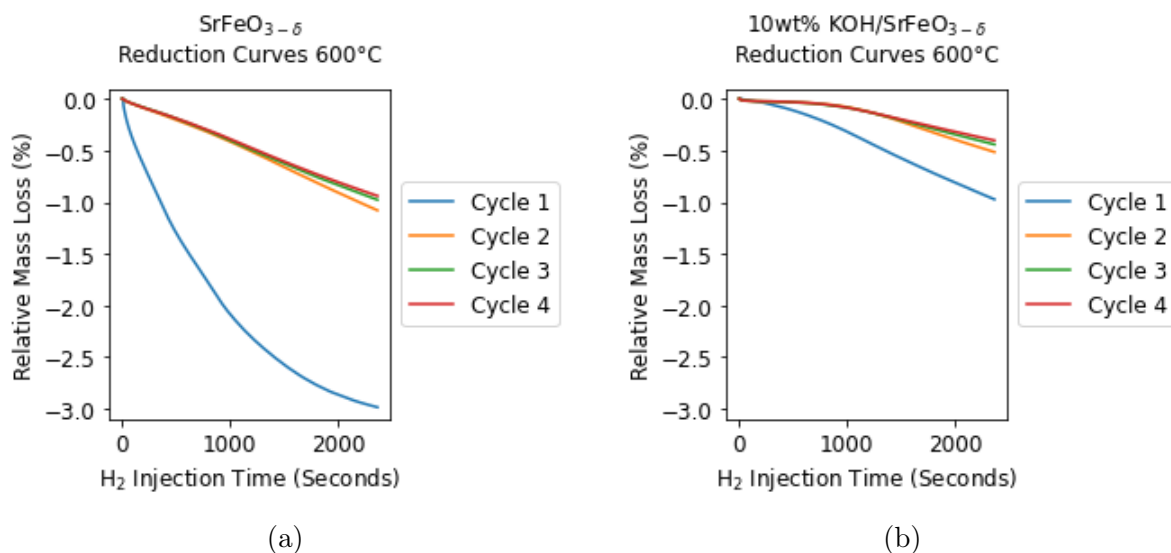


Figure 25: 600°C isotherm reduction relative mass loss curves for (a) SrFeO_{3-δ} (b) 10 wt% KOH/SrFeO_{3-δ}

The thiele moduli for the SrFeO_{3-δ} pellet were also calculated to better understand the design of the pellet. The thiele moduli were considered at the start ($t=0\text{s}$) and end ($t=2400\text{s}$) of the reduction reaction, for the 400°C, 500°C and 600°C isotherms. These thiele moduli results are summarised in Table 7 below. With the small magnitude of thiele

moduli present, this suggests that the pellet is not gas diffusion limited. This finding is in agreement with the Fe_2O_3 pellet design. And that the original of assumption of $\eta=1$ is validated. Furthermore, the small magnitude of the thiele moduli suggests that changing the OC material from Fe_2O_3 to $\text{SrFeO}_{3-\delta}$ is not significantly effecting the reaction rate, and that reactivity is still the limiting factor for the pellet. The undoped $\text{SrFeO}_{3-\delta}$ pellet has a reduced O_2 transfer ability in comparison to the Fe_2O_3 pellet, this is particularly noticeable at the 600°C isotherm (Figure 25 (a)). The 2400 H_2 injection, $\text{SrFeO}_{3-\delta}$ at 600°C achieves a steady state cyclic mass loss of 1wt% (Figure 23 (a)) in comparison to the Fe_2O_3 pellet achieving a mass loss of 2wt% (Figure 20 (a)).

Table 7: $\text{SrFeO}_{3-\delta}$ pellet thiele moduli at the start of the reduction cycle ($t=0\text{s}$) and at the end of the reduction cycle ($t=2400\text{s}$) for the 400°C, 500°C and 600°C isotherms.

$\text{SrFeO}_{3-\delta}$ Pellet	$t=0\text{s}$	$t=2400\text{s}$
400°C	2.2×10^{-5}	8.6×10^{-6}
500°C	2.1×10^{-5}	1.0×10^{-5}
600°C	2.4×10^{-5}	2.0×10^{-5}

The temperature dependent molecular diffusivities for 1.67% H_2 in N_2 were calculated to be: $D_{\text{mol},400^\circ\text{C}} = 3.15 \times 10^{-4} \frac{\text{m}^2}{\text{s}}$, $D_{\text{mol},500^\circ\text{C}} = 4.02 \times 10^{-4} \frac{\text{m}^2}{\text{s}}$, and $D_{\text{mol},600^\circ\text{C}} = 4.97 \times 10^{-4} \frac{\text{m}^2}{\text{s}}$. D_{eff} were dependent on the pellets porosities and tortuosity, highlighted in Table 4 and calculated using equation 21.

The poor O_2 transfer makes $\text{SrFeO}_{3-\delta}$ an unlikely choice for an OC in CLHP, with this current design of pellet. However, the long term cyclic stability of $\text{SrFeO}_{3-\delta}$ has suggested to be very stable in CLHP, more so than Fe_2O_3 [15].

The activation energy as a function of relative mass loss is plotted for the $\text{SrFeO}_{3-\delta}$ and 10wt% KOH/ $\text{SrFeO}_{3-\delta}$ pellets in Figure 26 below. The doping of 10wt% KOH is resulting in a significant energy barrier which needs to be overcome, to achieve depths of reduction beyond 0.02wt%. This significant energy barrier is related to the discussion earlier, where the presence of KOH is forming K_2CO_3 which may be inhibiting the overall reaction rate. Hence, this activation energy plot shows that doping of KOH onto $\text{SrFeO}_{3-\delta}$ is increasing the initial activation energy for the cyclic RWGS reaction, and should not be used to improve the reaction conversion. As for H_2 production, the KOH doped pellet should be further tested with a carbonaceous reducing species and oxidised in H_2O to understand the mechanism for CLHP.

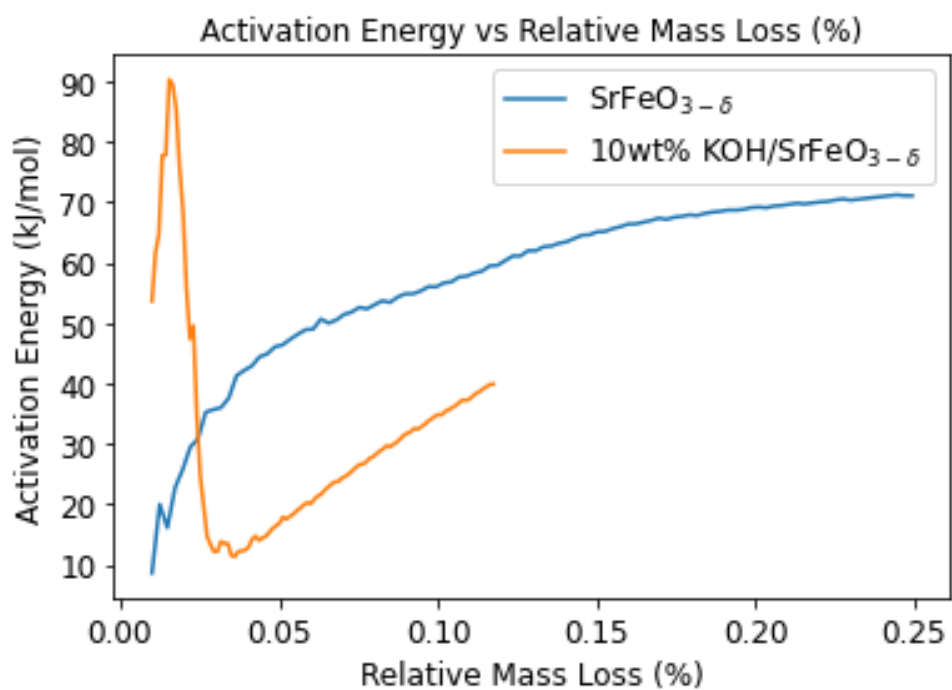


Figure 26: Activation Energy (kJ/mol) comparison of $\text{SrFeO}_{3-\delta}$ and 10wt% KOH/ $\text{SrFeO}_{3-\delta}$ pellets as a function of relative mass loss (%).

4.2.3 LaFeO_{3-δ} Pellet vs 10 wt% KOH/LaFeO_{3-δ} Pellet

The H₂ producing capability and redox stability of LaFeO_{3-δ} and 10wt% KOH/LaFeO_{3-δ} pellet samples were investigated at 300°C, 400°C, 500°C and 600°C (4 redox cycles per isotherm). The TGA relative mass change results are shown in Figure 27, with (a) displaying the undoped KOH pellet results and (b) displaying the 10wt% KOH doped pellet results. Figure 27 (a) and (b) show an initial mass loss upon heating to 300°C, likely due to the evaporation of H₂O.

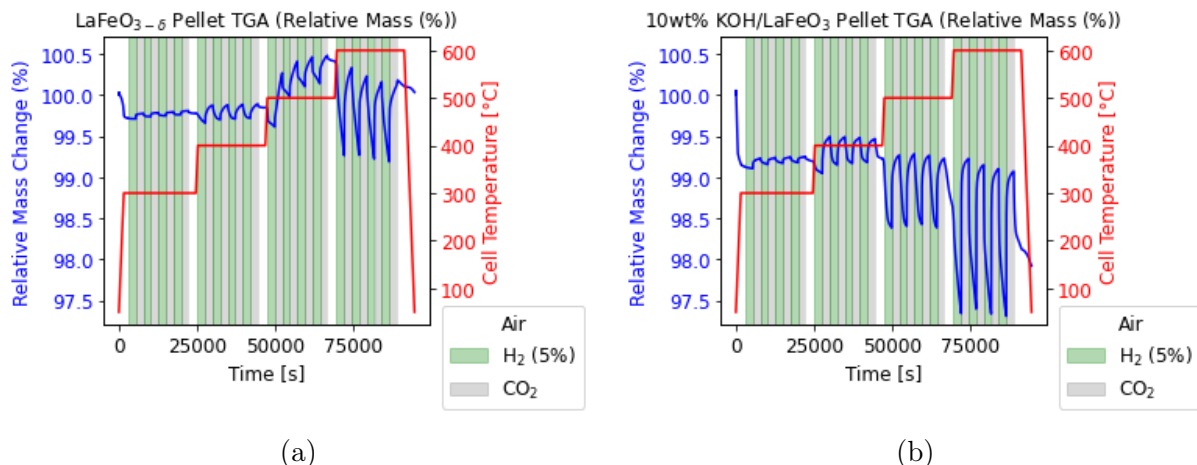


Figure 27: TGA cycles for (a) LaFeO_{3-δ} Pellet and (b) 10wt% KOH/LaFeO_{3-δ} Pellet. 4 redox cycle per isotherm: 300°C, 400°C, 500°C and 600°C

The undoped LaFeO_{3-δ} pellet (a) displays a steady state cycling behaviour at 300°C and 400°. The redox stability at the 500°C and 600°C do not originally start at a stable phase, yet after additional cycles, they would be expect to achieve a stable behaviour with no overall up or downwards drift. The 10wt% KOH/LaFeO_{3-δ} pellet however achieves a stable redox behaviour for each of the 4 isotherms.

Similarly to the Fe₂O₃ pellet and powder samples, the undoped LaFeO_{3-δ} and 10wt% KOH/LaFeO_{3-δ} pellets experience a 2 phase O₂ release behaviour. This 2 phase O₂ release can be seen by the 2 distinct gradients of relative mass loss in Figures 28 (b), 29 (a) and (b), and 30 (a) and (b) below.

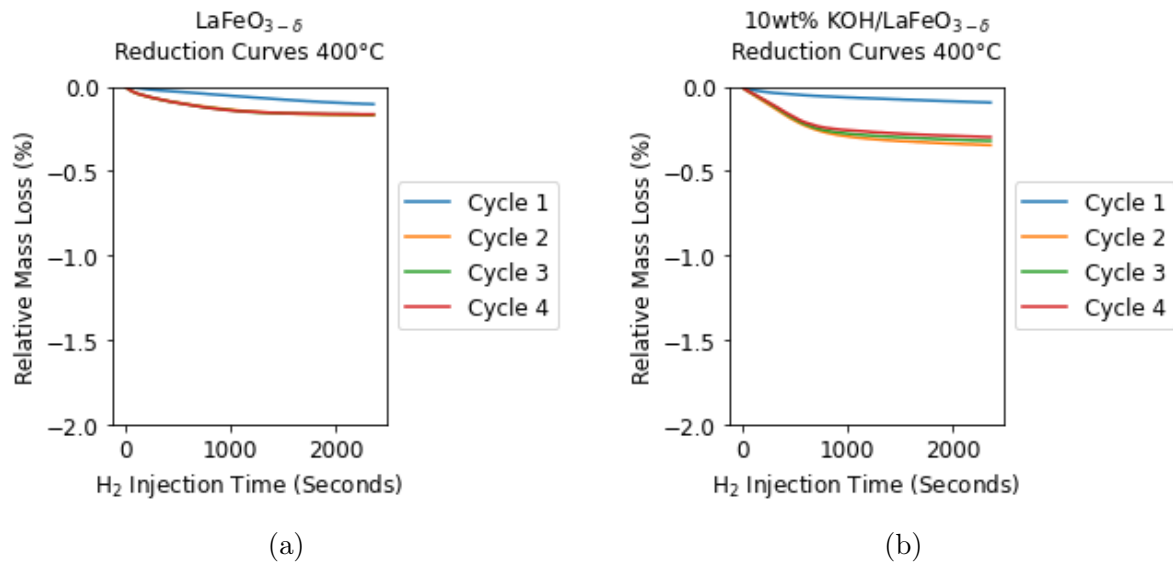


Figure 28: 400°C isotherm reduction conversion curves for (a) La $\text{FeO}_{3-\delta}$ (b) 10 wt% KOH/La $\text{FeO}_{3-\delta}$.

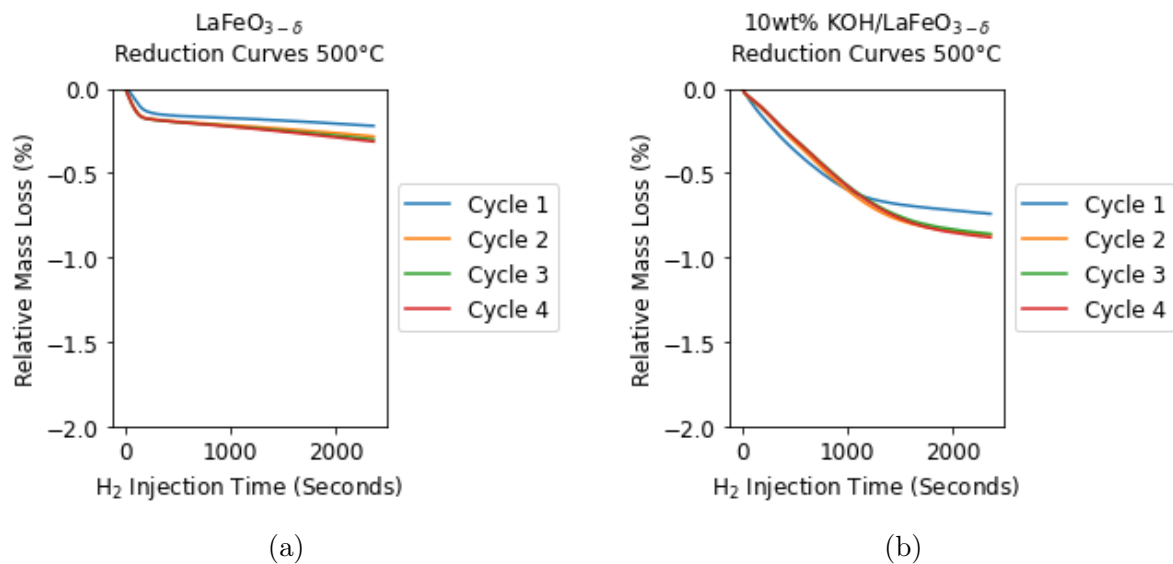


Figure 29: 500°C isotherm reduction conversion curves for (a) La $\text{FeO}_{3-\delta}$ (b) 10 wt% KOH/La $\text{FeO}_{3-\delta}$.

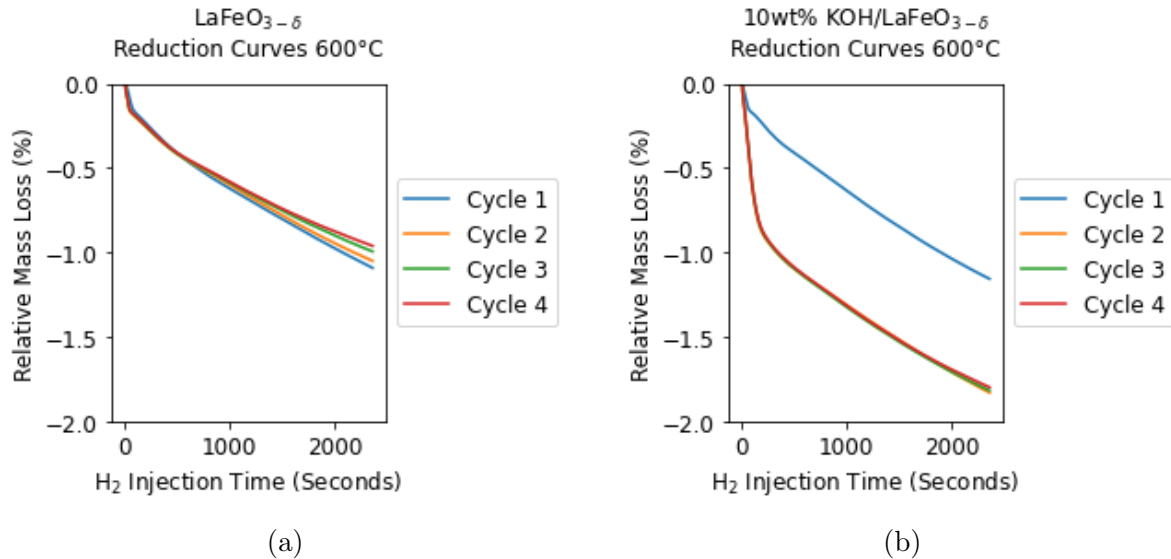


Figure 30: 600°C isotherm reduction conversion curves for (a) LaFeO_{3-δ} (b) 10 wt% KOH/LaFeO_{3-δ}.

This 2 phase O₂ release mechanism is not a consequence of the pellet design. The thiele moduli are shown in Table 8 below, and have small orders of magnitude suggesting that gas diffusion through the pellet is not limiting. Even when changing between Fe₂O₃, SrFeO_{3-δ}, and LaFeO_{3-δ}, the pellets are not limited by gas diffusion, but by the reactivity of the OC material itself.

Table 8: LaFeO_{3-δ} pellet thiele moduli at the start of the reduction cycle (t=0s) and at the end of the reduction cycle (t=2400s) for the 400°C, 500°C and 600°C isotherms.

Fe ₂ O ₃ Pellet	t=0s	t=2400s
400°C	2.7×10^{-5}	1.6×10^{-5}
500°C	4.4×10^{-5}	1.2×10^{-5}
600°C	6.2×10^{-5}	1.8×10^{-5}

The temperature dependent molecular diffusivities for 1.67% H₂ in N₂ were calculated to be: $D_{\text{mol},400^\circ\text{C}} = 3.15 \times 10^{-4} \frac{\text{m}^2}{\text{s}}$, $D_{\text{mol},500^\circ\text{C}} = 4.02 \times 10^{-4} \frac{\text{m}^2}{\text{s}}$, and $D_{\text{mol},600^\circ\text{C}} = 4.97 \times 10^{-4} \frac{\text{m}^2}{\text{s}}$. D_{eff} were dependent on the pellets porosities and tortuosity, highlighted in Table 4 and calculated using equation 21.

From the Figures 27, 28, 29, and 30 above, the depth of reduction, and the redox capacity is greater for the 10wt% KOH/LaFeO_{3-δ} pellet than for the LaFeO_{3-δ} pellet. However, as discussed in the 10wt% KOH/SrFeO_{3-δ} chapter prior, the KOH reacts with CO₂ to form carbonate through reaction 26. With 10wt% KOH doping, an additional relative mass fluctuation of ±5wt% could occur simply from the reforming of K₂CO₃ carbonates. However, the 10wt% KOH/LaFeO_{3-δ} (Figure 30 (b)) and the 10wt% KOH/SrFeO_{3-δ} (Figure 25 (b)) pellets cycling at the 600°C isotherm show unique and distinct behaviours. The 10wt% KOH/LaFeO_{3-δ} is forming K₂CO₃, this can be seen during the air injection

cycles at the end of each isotherm in Figure (27 (b)), in particular when the pellet loses significant mass in air. This mass loss is not associated with O₂ decoupling, as the undoped LaFeO_{3-δ} pellet does not experience any significant mass loss during the air injection at the end of each isotherm (Figure 27 (a)). This confirms that the greater redox capacity for the 10wt% KOH/LaFeO_{3-δ} pellet is a result of the K₂CO₃ carbonates reforming. However the reasons for LaFeO_{3-δ} and SrFeO_{3-δ} having different reduction behaviours is unclear. Whilst the K₂CO₃ carbonates were thought to block the pores and inhibit gas diffusion for the 10wt% KOH/SrFeO_{3-δ} pellet, this is not the case for the 10wt% KOH/LaFeO_{3-δ}. With LaFeO_{3-δ} pellets having a greater porosity ($\epsilon=0.00138$, Table 4) than the SrFeO_{3-δ} pellets ($\epsilon=0.00126$, Table 4), this could allow for gas diffusion throughout the LaFeO_{3-δ} to occur even with the formation of K₂CO₃. However, this argument is weak because: 1. the porosities of the 2 pellets are still small in magnitude and comparatively similar in scale. 2. the lack of control from wet impregnation will have resulted in the pellet with the greater porosity receiving a greater KOH wt% doping. There is little-to-no literature regarding KOH doping into perovskites for chemical looping purposes, so this reaction mechanism is not well understood.

The activation energy as a function of relative mass loss is plotted for the LaFeO_{3-δ} and 10wt% KOH/LaFeO_{3-δ} pellets in Figure 31 below. For the undoped LaFeO_{3-δ} sample there are 2 distinct energy levels associated with the relative mass loss, this directly relates to the 2 phase O₂ release mechanism discussed above. The relative mass loss at which the 2nd energy barrier starts to become present is at 0.19wt%. The 10wt% KOH/LaFeO_{3-δ} activation energy profile only shows a single energy barrier being present at $\sim 130\text{ kJ/mol}$, whilst the reduction mass loss curves for the 500°C (Figure 29 (b)) and 600°C (Figure 30 (b)) isotherms show a 2 phase O₂ release mechanism. This is not displayed on the activation energy plot below simply due to the range for which relative mass loss is plotted. If the TGA reduction cycles were increased from 2400s, this would allow for the activation energy to be plotted for a greater range of relative mass loss. The 2nd phase energy level would start to become noticeable at $\sim 0.85\text{wt\%}$.

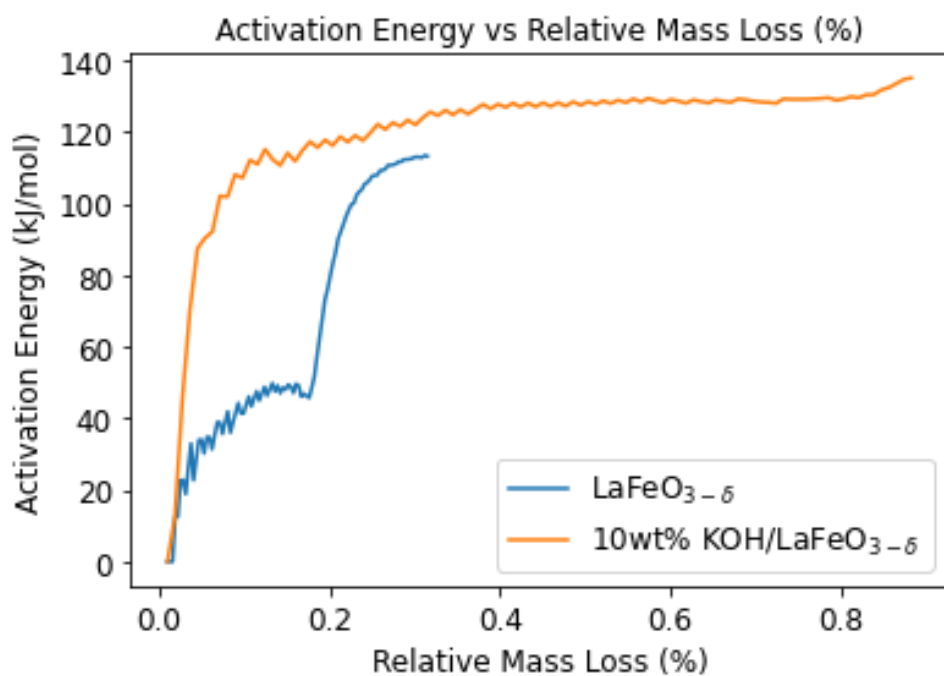


Figure 31: Activation Energy (kJ/mol) comparison of LaFeO_{3-δ} and 10wt% KOH/LaFeO_{3-δ} pellets as a function of relative mass loss (%).

4.2.4 1LaFeO_{3-δ}:9Fe₂O₃ Pellet vs 10wt% KOH/1LaFeO_{3-δ}:9Fe₂O₃ Pellet

The H₂ producing capability and redox stability of 1LaFeO_{3-δ}:9Fe₂O₃ and 10wt% KOH/1LaFeO_{3-δ}:9Fe₂O₃ pellet samples were investigated at 300°C, 400°C, 500°C and 600°C (4 redox cycles per isotherm). The TGA relative mass change results are shown in Figure 32, with (a) displaying the undoped KOH pellet results and (b) displaying the 10wt% KOH doped pellet results. Figure 32 (b) show an initial mass loss upon heating to 300°C, likely due to the evaporation of H₂O.

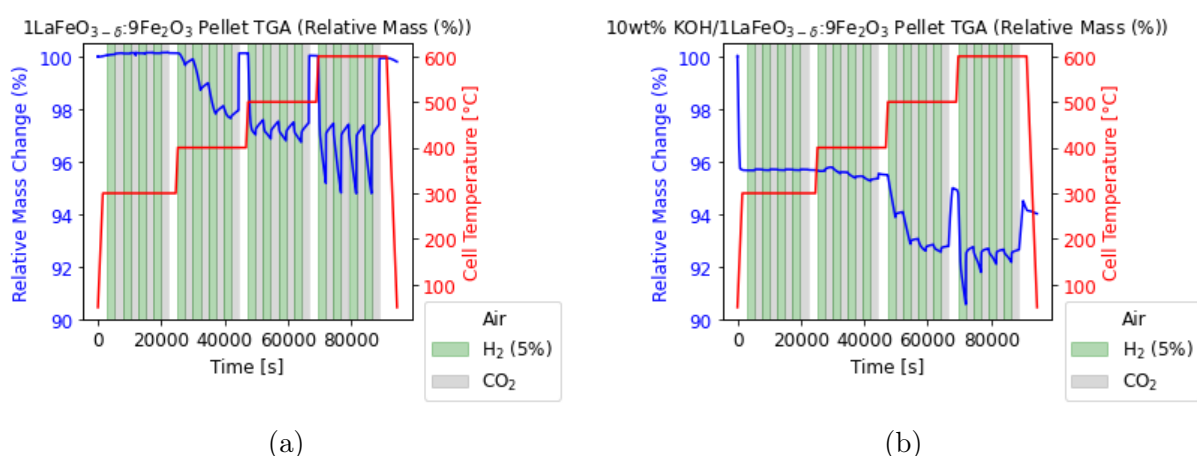


Figure 32: TGA cycles for (a) 1LaFeO_{3-δ}:9Fe₂O₃ Pellet and (b) 10wt% 1LaFeO_{3-δ}:9Fe₂O₃ Pellet.

Each of the pellets operating at the 300°C isotherm experience minimal mass transfer per redox cycle. However, at 400°C the 1LaFeO_{3-δ}:9Fe₂O₃ pellet is oxidising in the presence of CO₂. This is not unexpected as Fe₂O₃ pellets were found to oxidise in an earlier chapter at 400°C. The 10wt% KOH/1LaFeO_{3-δ}:9Fe₂O₃ experience a decreased depth of reduction per cycle in comparison to its undoped counter part, this is shown in Figure 33 below.

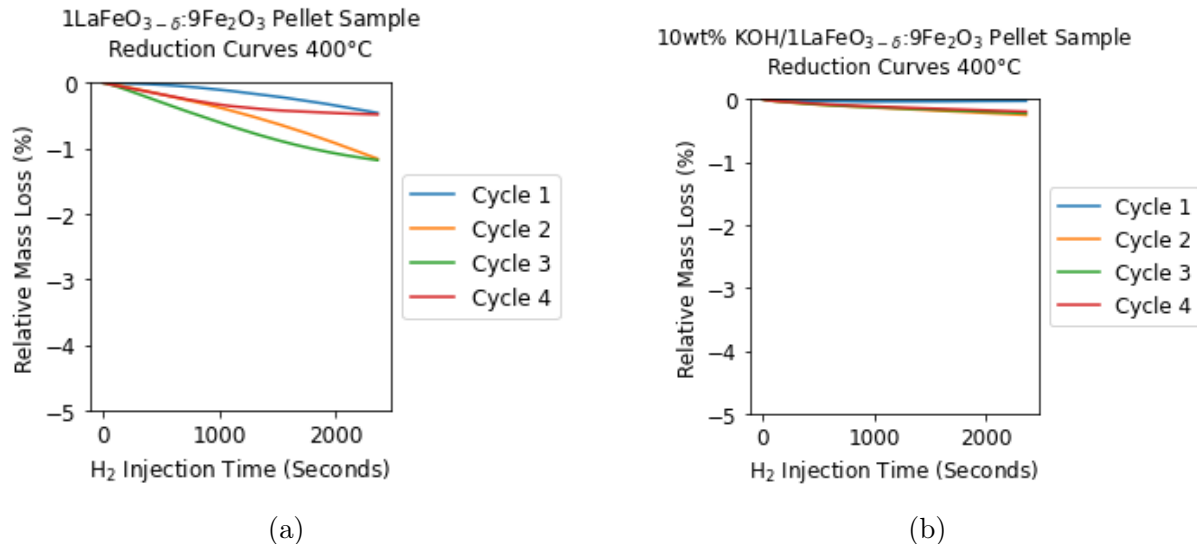


Figure 33: 400°C isotherm reduction conversion curves for (a) 1LaFeO_{3-δ}:9Fe₂O₃ (b) 10 wt% KOH/1LaFeO_{3-δ}:9Fe₂O₃

During the 500°C and 600°C isotherms, the 1LaFeO_{3-δ}:9Fe₂O₃ pellet is experiencing a stable cyclic behaviour, whilst the 10wt% KOH/1LaFeO_{3-δ}:9Fe₂O₃ pellet is experiencing a degrading cyclic capacity (less mass transfer per reduction and oxidation) with each cycle. This behaviour is noticeable in Figure 32 (b) during the 500°C and 600°C isotherms, where the relative mass change per redox cycle is decaying. This can be further seen from the relative mass loss curves for the 10wt% KOH/1LaFeO_{3-δ}:9Fe₂O₃ pellet, with the decaying depth of reduction achieved with each successive cycle (Figure 34 (b) and Figure 35 (b)). This behaviour is more similar to the 10wt% KOH/SrFeO_{3-δ} pellet behaviour, in contrast to the 10wt% KOH/LaFeO_{3-δ} pellet. Whilst KOH is known to form K₂CO₃ in the presence of CO₂, when 10wt% KOH/1LaFeO_{3-δ}:9Fe₂O₃ is exposed to air it does not experience a significant mass loss, but it does seem to regenerate. The reaction mechanism is being inhibited by the introduction of KOH. As a result, doping of 10wt% KOH to 1LaFeO_{3-δ}:9Fe₂O₃ is not recommended for improving the cyclic RWGS reaction rate.

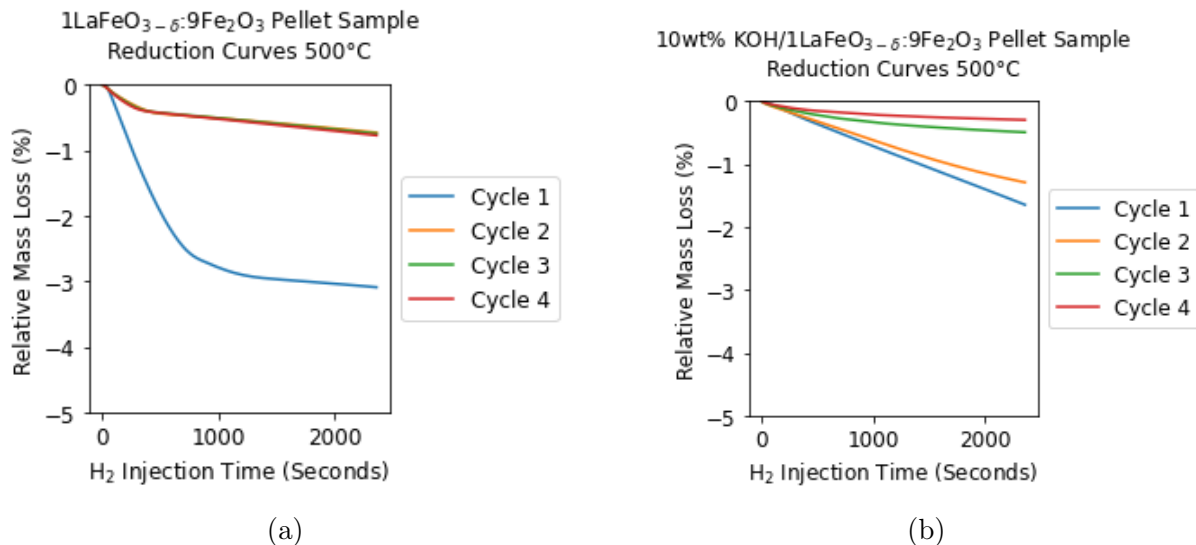


Figure 34: 500°C isotherm reduction relative mass loss curves for (a) 1LaFeO_{3- δ} :9Fe₂O₃ (b) 10 wt% KOH/1LaFeO_{3- δ} :9Fe₂O₃

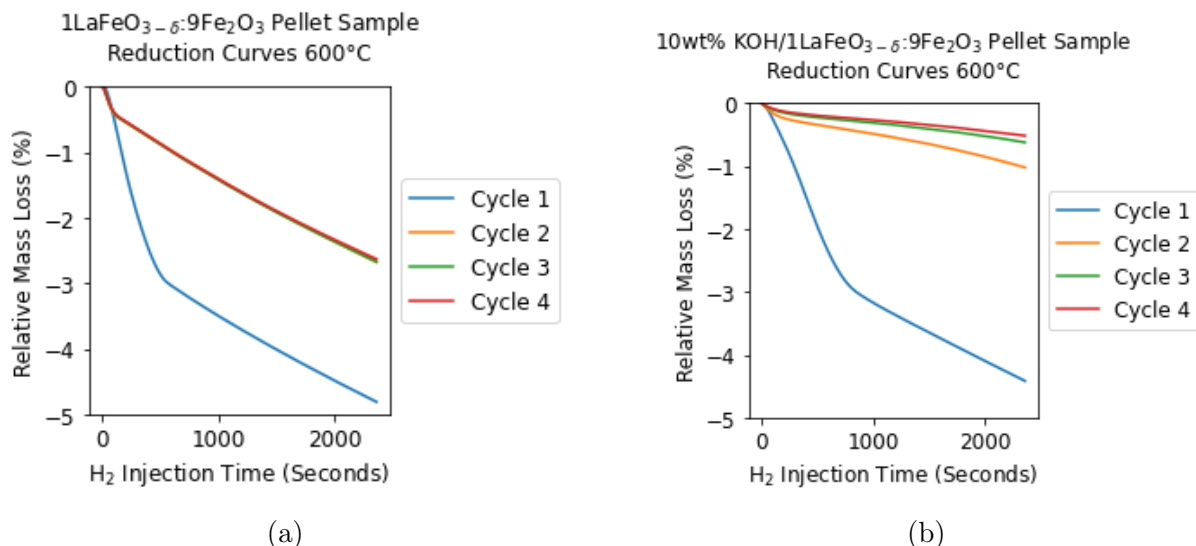


Figure 35: 600°C isotherm reduction relative mass loss curves for (a) 1LaFeO_{3- δ} :9Fe₂O₃ (b) 10 wt% KOH/1LaFeO_{3- δ} :9Fe₂O₃

The thiele moduli for the 1LaFeO_{3- δ} :9Fe₂O₃ pellet at the start and end of the reduction reactions, for the 400°C, 500°C, and 600°C are shown in Table 9. With the small magnitudes, the reactivity of the OC material is not significant and still remains the limiting factoring effecting the overall reaction rate. Gas diffusion throughout the pellet is not limiting.

Table 9: 1LaFeO_{3-δ}:9Fe₂O₃ pellet thiele moduli at the start of the reduction cycle (t=0s) and at the end of the reduction cycle (t=2400s) for the 400°C, 500°C and 600°C isotherms.

Fe ₂ O ₃ Pellet	t=0s	t=2400s
400°C	2.9×10^{-5}	1.6×10^{-5}
500°C	4.0×10^{-5}	1.4×10^{-5}
600°C	6.2×10^{-5}	2.9×10^{-5}

The temperature dependent molecular diffusivities for 1.67% H₂ in N₂ were calculated to be: $D_{\text{mol},400^\circ\text{C}} = 3.15 \times 10^{-4} \frac{\text{m}^2}{\text{s}}$, $D_{\text{mol},500^\circ\text{C}} = 4.02 \times 10^{-4} \frac{\text{m}^2}{\text{s}}$, and $D_{\text{mol},600^\circ\text{C}} = 4.97 \times 10^{-4} \frac{\text{m}^2}{\text{s}}$. D_{eff} were dependent on the pellets porosities and tortuosity, highlighted in Table 4 and calculated using equation 21.

The activation energy as a function of relative mass loss is plotted for the 1LaFeO_{3-δ}:9Fe₂O₃ and 10wt% KOH/1LaFeO_{3-δ}:9Fe₂O₃ pellets in Figure 36 below. For the undoped 1LaFeO_{3-δ}:9Fe₂O₃ pellet there are 2 distinct energy levels associated with the relative mass loss. The relative mass loss at which the 2nd energy barrier starts to become present is at 0.44wt%. The 10wt% KOH/1LaFeO_{3-δ}:9Fe₂O₃ activation energy profile shows an interesting trend. Whilst the activation energy for the 10wt% KOH/1LaFeO_{3-δ}:9Fe₂O₃ is calculated to be less than its undoped equivalent, these values are likely miss leading. Besides 10wt% KOH/1LaFeO_{3-δ}:9Fe₂O₃ having a lower activation energy, what must also be considered is its unstable, degrading redox capacity. The degrading cyclic behaviour experienced at the 500°C and 600°C isotherm does not provide consistent data to the isomass method. Extending beyond 4 cycles, to the point where the redox capacity is truly negligible (stabilised after sufficient cycles), then a more accurate activation energy profile can be expected for the 10wt% KOH/1LaFeO_{3-δ}:9Fe₂O₃ pellet.

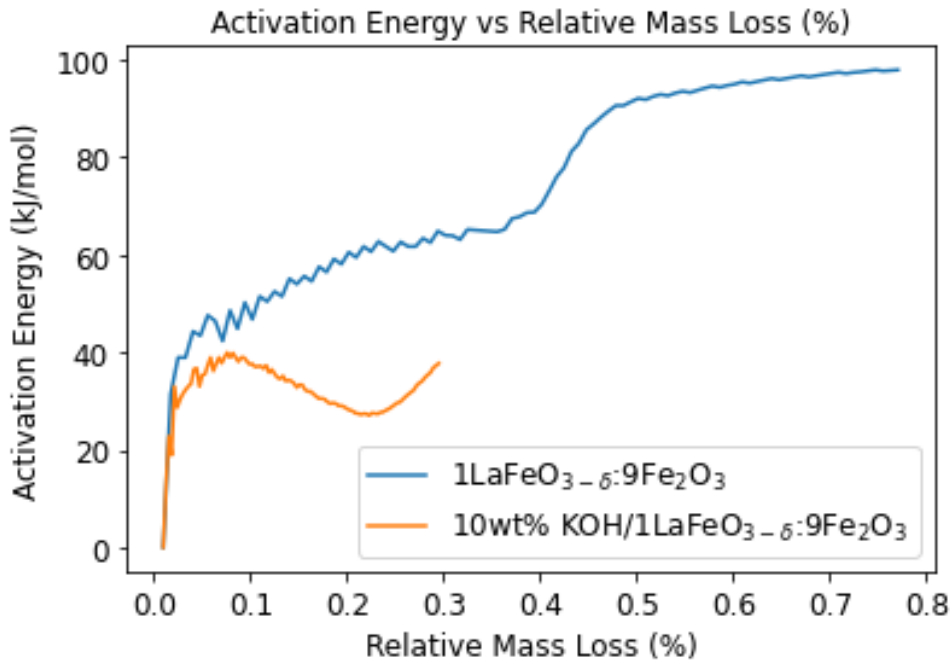


Figure 36: Activation Energy (kJ/mol) comparison of $1\text{LaFeO}_{3-\delta}:9\text{Fe}_2\text{O}_3$ and 10wt% KOH/ $1\text{LaFeO}_{3-\delta}:9\text{Fe}_2\text{O}_3$ pellets as a function of relative mass loss (%).

4.3 Packed Bed Reactor

Figure 37 displays the exhaust stream composition from the PBR, which operated at 490°C and $P=1\text{atm}$. 2 cycles of cyclic RWGS were completed, the 1st cycle had injection periods of 240 seconds H_2 (5%) followed by 240 seconds of CO_2 , the 2nd cycle had injection periods of 900 seconds H_2 (5%) followed by 900 seconds of CO_2 . N_2 purge gas was injected between cycles. Each gas had a volumetric flow rate of 2 L/min .

With the exhaust stream measure by ABB EL3020, the following equation can be used to consider the moles of H_2 consumed during a RWGS reduction cycle:

$$\text{moles}_{\text{H}_2,\text{consumed}} = \int_{t_{\text{start}}}^{t_{\text{end}}} (x_{\text{H}_2,\text{blank}} - x_{\text{H}_2,\text{exp}}) \cdot \dot{V}_{\text{flow},\text{H}_2} \cdot \frac{\rho_{\text{H}_2}}{mr_{\text{H}_2}} dt \quad (27)$$

Where t_{start} is the start of the H_2 reduction phase, t_{end} is the end of the H_2 reduction phase, $x_{\text{H}_2,\text{blank}}$ is the mole fraction of H_2 when no reaction is taking place, $x_{\text{H}_2,\text{exp}}$ is the mole fraction of H_2 during the reaction, $\dot{V}_{\text{flow},\text{H}_2}$ is the volume flow rate of H_2 into the reactor ($\frac{\text{m}^3}{\text{s}}$), ρ_{H_2} is the density of H_2 at $T = 490^\circ\text{C}$ and $P = 1 \text{ atm}$ ($\frac{\text{g}}{\text{m}^3}$), mr_{H_2} is the molar mass of H_2 ($\frac{\text{g}}{\text{mol}}$).

A similar equation can be applied to the consumption of CO_2 (switching the species from H_2 to CO_2) for the oxidation cycle of the RWGS:

$$\text{moles}_{\text{CO}_2, \text{consumed}} = \int_{t_{\text{start}}}^{t_{\text{end}}} (x_{\text{CO}_2, \text{blank}} - x_{\text{CO}_2, \text{exp}}) \cdot \dot{V}_{\text{flow, CO}_2} \cdot \frac{\rho_{\text{CO}_2}}{mr_{\text{CO}_2}} dt \quad (28)$$

Calibration and zero testing of the PBR were completed at 20°C, the H₂ volume composition was measured to be 5% as expected, and the CO₂ was measured at 100%. During operation at 490°C, the H₂ was being consumed by the OC, forming H₂O and consequently reducing the OC. The CO₂ was also being consumed, forming CO and consequently oxidising the OC. However, the results from the CO₂ oxidation are likely to be inaccurate. The moles of O₂ decoupled (during cycle 2, 900 seconds of H₂ reduction) from the 113.19grams of OC in the reactor bed is calculated to be 0.0042mol (calculated based on the moles of H₂ consumed using equation 27), resulting in a 0.117wt% relative mass loss of the OC. Assuming the OC pellets react homogeneously throughout the bed, the relative mass of the OC should now be 99.883wt%. FeO forms when a relative mass of 96.667wt% has been achieved. This is not the case, and with Fe₃O₄ oxidising and reaching an equilibrium, there will be minimal formation of CO at 490°C (equilibrium for Fe₃O₄ and Fe₂O₃ at 490°C: $\frac{P_{\text{CO}}}{P_{\text{CO}_2}} = 2.1 \times 10^{-6}$). Consequently, the CO and CO₂ profiles are more likely to be an artifact, rather than any insightful information. There is possibly crosstalk, as the CO presence is only there when the CO₂ is injected. Additionally, the reactor is made of iron, and is possibly oxidising in the presence of CO₂, which further adds complication to the exhaust CO₂ and CO streams.

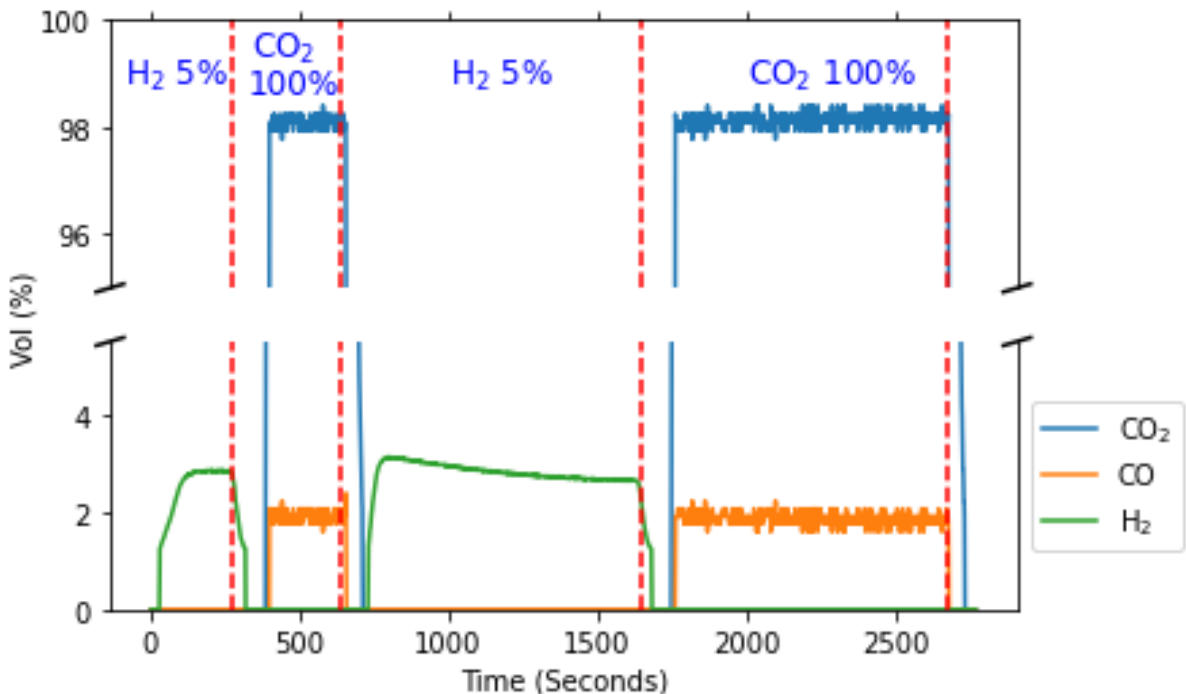


Figure 37: PBR at 490°C bed temperature and P=1atm. 113.19g of 1LaFeO_{3-δ}:9Fe₂O₃ oxygen carrier. 5% H₂ is the reducing agent. CO₂ is the oxidising agent. Exhaust gas composition measured using the ABB EL3020, specifically for species; CO₂, CO, H₂.

If the OC is truly being oxidised, where this oxidation data cannot be seen on Figure 37 due to the possibility of an artifact or the reactor itself oxidising. Then oxidising with only a relative mass of 99.883wt% suggests that the OC in the bed is not reacting homogeneously. The possibility of what an inhomogeneous reactor bed looks like with an equilibrium gradient present, is shown in Figure 38. However, until the measurements for CO₂ and CO are understood and explainable, then this is not conclusive information.

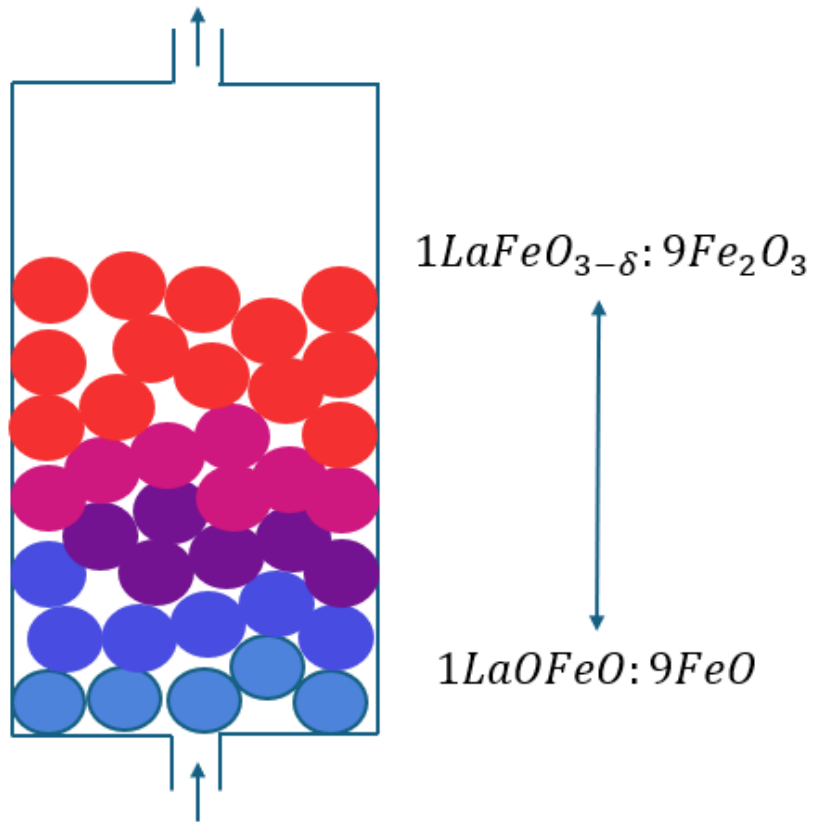


Figure 38: Example of a equilibrium gradient within the PBR, where the OC does not redox homogeneously.

5. Limitations and considerations of the RWGS proxy for H_2 Production Testing

Whilst testing for a materials ability to produce H_2 was carried out using cyclic RWGS, there are some considerations which must be made about the results.

- The use of RWGS needs to be carefully considered when testing with various dopants, for the possibility of forming carbonates which can influence the redox results of the O_2 decoupling. This was identified when using KOH dopant with the oxidising agent of CO_2 , where the improved relative mass transfer was largely a result of the forming and deforming of carbonates (K_2CO_3) and not O_2 transfer. The true effect of KOH doping should be tested in a CLHP environment with a carbonaceous reducing agent species and H_2O as the oxidising agent, to accurately understand the effects of KOH doping for H_2 production. A potential example would be the cyclic water gas shift, in contrast to the cyclic reverse water gas shift which was tested in this project.
- Any potential OC must be tested in the presence of a carbonaceous reducing species followed by H_2O oxidisation. When using RWGS, the reducing agent of H_2 will not result in coking of the OC, hence the RWGS will not allow for a true representation of an OC ability in CLHP practices. However RWGS is still beneficial when comparing a range of various OCs ability to reduce and oxidise, and under what operating conditions.
- For the operating temperatures in this project (<850K), the reducing strength of H_2 is weaker than the reducing strength of CO. This can be determined by the water gas shift equilibrium constants. The results for the reduction of OCs are based on H_2 reducing agent, the use of CO will likely achieve a greater depth of reduction on a per mole basis.

6. Conclusion

The objective of this project was to investigate various OC materials for H₂ production capability at low temperatures (tested using RWGS as a proxy). A secondary objective was to scale the technology from a small scale TGA reaction, to a larger scale packed bed reactor.

Firstly the perovskites of SrFeO_{3-δ} and LaFeO_{3-δ} were successfully produced by the solid state synthesis preparation method, and accurately characterised using X-ray diffraction, and Rietveld Refinement phase identification.

Secondly, a thermogravimetric analyser was used to test for H₂ producing ability at a range of temperatures using a cyclic procedure of the RWGS. A comparison between pelletised and powder samples of Fe₂O₃ shown that pelletisation did result in gas diffusion limitations, instead the reactivity of the pellet material itself was found to be limiting the overall reaction, this was determined from the small magnitudes of the thiele modulus. The LaFeO_{3-δ}, SrFeO_{3-δ}, and 1LaFeO_{3-δ}:9Fe₂O₃ pellets all had thiele moduli with small magnitudes, confirming that the pellet design is not gas diffusion limited. Whilst the various oxygen carrier materials did not experience a H₂ producing capacity at 300°C, it was shown that the Fe₂O₃, LaFeO_{3-δ}, and 1LaFeO_{3-δ}:9Fe₂O₃O pellets do have a H₂ producing capacity at 400°C and above, whilst SrFeO_{3-δ} was not found to be H₂ producing at 400°C. The SrFeO_{3-δ} pellet was found to have a H₂ producing ability between 500-600°C. The 10wt% KOH/SrFeO_{3-δ} pellet experienced an inhibited reaction behaviour, particularly at higher temperatures (600°C), with the possible explanation being a result of carbonates forming and blocking the pores of the pellet. The 10wt% KOH/LaFeO_{3-δ} pellet experienced an increased redox capacity in comparison to its undoped counterpart, yet this was found to be a result of the KOH forming carbonates, where 10wt% KOH doping can correspond to a ±5wt% change through the reforming of K₂CO₃. The 10wt% KOH/1LaFeO_{3-δ}:Fe₂O₃ pellet experienced a degraded redox capacity, which was more noticeable at the higher temperatures (500°C and 600°C). However this pellet could be regenerated under a cycle in air at high temperatures (>600°C). Overall Fe₂O₃ pellets had the greatest redox capacity for all temperatures tested.

Thirdly, the packed bed reactor was assembled successfully, and tested on a scale with 113.19g of oxygen carrier material. Whilst the injected H₂ was found to be partially consumed, the CO₂ and CO data which mis-leading, likely as a result of being an artifact.

As the pellet design was found to be not diffusion limited, further research must be complete by testing alternative oxygen carrier materials and dopants. Particularly testing materials for an increased redox capacity, and redox stability at low temperatures (\leq 500°C). Redox stability can be tested by trialling more cycles, and with greater injection

periods for the reducing and oxidising agents. Furthermore, whilst the KOH doping was found to inhibit some materials reactivity, it should be tested in a cyclic water-gas shift reaction to better understand the potential of KOH doping in chemical looping hydrogen production.

References

1. Moore J, Durham J, Eijk A, Karakas E, Kurz R, Lesak J, McBain M, McCalley P, Moroz L, Mohamed Z, Pettinato B, Phillipi G, Watanabe H and Williams B. Compressors and expanders. *Machinery and Energy Systems for the Hydrogen Economy* 2022 Jan :333–424. DOI: 10.1016/B978-0-323-90394-3.00002-3
2. Lane H. lane hydrogen | cubic feet | producer gas | 1909 | 0522 | Flight Archive. 1908. Available from: <https://web.archive.org/web/20090504030718/http://www.flightglobal.com/pdfarchive/view/1909/1909%20-%200522.html>
3. Messerschmitt A. UNITED STATES PATENT OFFICE. United States Patent Office 1910 :1–3. Available from: <https://patentimages.storage.googleapis.com/f0/21/98/1f1ad50622b1ae/US971206.pdf>
4. Reed HC and Berg CHO. Hydrogen process. 1948 Jul
5. Schmidt C, Shi H, Maiti D, Hare BJ, Bhethanabotla VR and Kuhn JN. Chemical looping approaches to decarbonization via CO₂ repurposing. *Discover Chemical Engineering* 2023 3:1 2023 Aug; 3:1–24. DOI: 10.1007/S43938-023-00030-9. Available from: <https://link.springer.com/article/10.1007/s43938-023-00030-9>
6. Vos YD, Jacobs M, Voort PVD, Driessche IV, Snijkers F and Verberckmoes A. Development of Stable Oxygen Carrier Materials for Chemical Looping Processes—A Review. *Catalysts* 2020, Vol. 10, Page 926 2020 Aug; 10:926. DOI: 10.3390/CATAL10080926. Available from: <https://www.mdpi.com/2073-4344/10/8/926> <https://www.mdpi.com/2073-4344/10/8/926>
7. Zhang J, Cui Y, Si-ma W, Zhang Y, Gao Y, Wang P and Zhang Q. Advances and Challenges in Oxygen Carriers for Chemical Looping Partial Oxidation of Methane. *Catalysts* 2024, Vol. 14, Page 246 2024 Apr; 14:246. DOI: 10.3390/CATAL14040246. Available from: <https://www.mdpi.com/2073-4344/14/4/246> <https://www.mdpi.com/2073-4344/14/4/246>
8. Feng Y, Wang N, Guo X and Zhang S. Dopant screening of modified Fe₂O₃ oxygen carriers in chemical looping hydrogen production. *Fuel* 2020 Feb; 262:116489. DOI: 10.1016/J.FUEL.2019.116489
9. Dawa T and Sajjadi B. Exploring the potential of perovskite structures for chemical looping technology: A state-of-the-art review. *Fuel Processing Technology* 2024 Jan; 253:108022. DOI: 10.1016/J.FUPROC.2023.108022
10. Görke RH, Marek EJ, Donat F and Scott SA. Reduction and oxidation behavior of strontium perovskites for chemical looping air separation. *International Journal of Greenhouse Gas Control* 2020 Mar; 94:102891. DOI: 10.1016/J.IJGGC.2019.102891

11. Zhou Y, Herz LM, Jen AKY and Saliba M. Advances and challenges in understanding the microscopic structure–property–performance relationship in perovskite solar cells. *Nature Energy* 2022 Sep; 7:794–807. DOI: 10.1038/s41560-022-01096-5
12. Capstick S, Bulfin B, Naik JM, Gigantino M and Steinfeld A. Oxygen separation via chemical looping of the perovskite oxide Sr_{0.8}Ca_{0.2}FeO₃ in packed bed reactors for the production of nitrogen from air. *Chemical Engineering Journal* 2023 Jan; 452:139289. DOI: 10.1016/J.CEJ.2022.139289
13. Krizhevsky A, Sutskever I and Hinton GE. Imagenet classification with deep convolutional neural networks. *Advances in Neural Information Processing Systems*. 2012 :1097–105
14. Götsch T, Schlicker L, Bekheet MF, Doran A, Grünbacher M, Praty C, Tada M, Matsui H, Ishiguro N, Gurlo A, Klötzer B and Penner S. Structural investigations of La_{0.6}Sr_{0.4}FeO₃– δ under reducing conditions: kinetic and thermodynamic limitations for phase transformations and iron exsolution phenomena. *RSC Advances* 2018 Jan; 8:3120–31. DOI: 10.1039/C7RA12309D. Available from: <https://pubs.rsc.org/en/content/articlehtml/2018/ra/c7ra12309d%20https://pubs.rsc.org/en/content/articlelanding/2018/ra/c7ra12309d>
15. Marek E, Hu W, Gaultois M, Grey CP and Scott SA. The use of strontium ferrite in chemical looping systems. *Applied Energy* 2018 Aug; 223:369–82. DOI: 10.1016/J.APENERGY.2018.04.090
16. Ma Z, Xiao R and Chen L. Redox reaction induced morphology and microstructure evolution of iron oxide in chemical looping process. *Energy Conversion and Management* 2018 Jul; 168:288–95. DOI: 10.1016/J.ENCONMAN.2018.05.013
17. Zheng H, Jiang ·X, Gao Y, Tong ·A and Liang Zeng ·. Chemical looping reforming: process fundamentals and oxygen carriers. *Discover Chemical Engineering* 2022 2:1 2022 Jul; 2:1–50. DOI: 10.1007/S43938-022-00012-3. Available from: <https://link.springer.com/article/10.1007/s43938-022-00012-3>
18. Voitic G and Hacker V. Recent advancements in chemical looping water splitting for the production of hydrogen. *RSC Advances* 2016 Oct; 6:98267–96. DOI: 10.1039/C6RA21180A. Available from: <https://pubs.rsc.org/en/content/articlehtml/2016/ra/c6ra21180a%20https://pubs.rsc.org/en/content/articlelanding/2016/ra/c6ra21180a>
19. De Filippis P, D’Alvia L, Damizia M, Caprariis B and Del Prete Z. Pure hydrogen production by steam-iron process: The synergic effect of MnO₂ and Fe₂O₃. *International Journal of Energy Research* 2021 Mar; 45:4479–94. DOI: 10.1002/er.6117
20. NASA C. Chemical Equilibrium with Applications | Glenn Research Center | NASA. 2002. Available from: <https://www1.grc.nasa.gov/research-and-engineering/ceaweb/>

21. Toby BH and Von Dreele RB. <i>GSAS-II</i> : the genesis of a modern open-source all purpose crystallography software package. *Journal of Applied Crystallography* 2013 Apr; 46:544–9. DOI: 10.1107/S0021889813003531
22. Fuller E, Schettler P and Giddings J. A new method for the prediction of binary gas-phase diffusion coefficients. *Industrial & Engineering Chemistry* 1966 May; 58:19–27
23. Prieur J, Plessis DU and Masliyah JH. Mathematical Modelling of Flow Through Consolidated Isotropic Porous Media. *Transport in Porous Media* 1988; 3:145–61
24. Zhao LJ and Sun Q. Calculations of effectiveness factors and the criteria of mass transfer effect for high-temperature methanation (HTM) catalyst. DOI: 10.1093/ijlct/ctu005. Available from: <https://academic.oup.com/ijlct/article/10/3/288/705082>
25. Rini AS and Restiana S. Diffraction Pattern Simulation of Crystal Structure towards the Ionic Radius Changes Via Vesta Program. *Journal of Technomaterials Physics* 2019; 01:132–9
26. Shannon RD. Revised Effective Ionic Radii and Systematic Studies of Interatomic Distances in Halides and Chalcogenides. *Acta Cryst* 1976; 32:751
27. Chen T, Foo C, Chi S and Tsang E. Interstitial and substitutional light elements in transition metals for heterogeneous catalysis. 2021. DOI: 10.1039/d0sc06496c
28. Leineweber A, Gressmann T, Nikolussi M and Mittemeijer EJ. The hkl dependences of microstrain and of macrostress-induced macrostrain; a comparison for intrinsically extremely anisotropic cementite, Fe 3C. *Zeitschrift fur Kristallographie, Supplement* 2009 :103–8. DOI: 10.1524/zksu.2009.0015. Available from: https://www.researchgate.net/publication/250976467_The_hkl_dependences_of_microstrain_and_of_macrostress-induced_macrostrain_a_comparison_for_intrinsically_extremely_anisotropic_cementite_Fe_3_C
29. Spreitzer D and Schenk J. Reduction of Iron Oxides with Hydrogen—A Review. *Steel Research International* 2019 Oct; 90. DOI: 10.1002/SRIN.201900108
30. Harrison AR, Kwong KY, Zheng Y, Balkrishna A, Dyson A and Marek EJ. Kinetic and Thermodynamic Enhancement of Low-Temperature Oxygen Release from Strontium Ferrite Perovskites Modified with Ag and CeO₂. *Energy and Fuels* 2023 Jul; 37:9487–99. DOI: 10.1021/ACS.ENERGYFUELS.3C01263/SUPPL{_}FILE/EF3C01263{_}SI{_}001.PDF. Available from: /pmc/articles/PMC10331733/%20/pmc/articles/PMC10331733/?report=abstract%20<https://www.ncbi.nlm.nih.gov/pmc/articles/PMC10331733/>
31. Šimon P. ISOCONVERSIONAL METHODS Fundamentals, meaning and application. *Journal of Thermal Analysis and Calorimetry* 2004; 76:123–32

32. Firman N, Noor A, Zakir M, Maming M and Fathurrahman A. Absorption of Carbon Dioxide into Potassium Hydroxide: Preliminary Study for its Application into Liquid Scintillation Counting Procedure. *Egyptian Journal of Chemistry* 2021 Apr; 0:0–0. DOI: [10.21608/ejchem.2021.66304.3506](https://doi.org/10.21608/ejchem.2021.66304.3506)
33. Pełech I, Staciwa P, Sibera D, Pełech R, Sobczuk KS, Kayalar GY, Narkiewicz U and Cormia R. CO₂ Adsorption Study of Potassium-Based Activation of Carbon Spheres. *Molecules* (Basel, Switzerland) 2022 Aug; 27. DOI: [10.3390/molecules27175379](https://doi.org/10.3390/molecules27175379)

Appendix

A. Mass Flow Controller Calibration Procedure

3 Bronkhorst EL-FLOW select F-201CV mass flow controllers were used to control the gas inlet feed, they are originally designed for H₂, N₂, and CO. The CO calibrated MFC had to be re-adjusted to allow for CO₂ mass flow (as this is the oxidising agent used in this project). As they operate using the Bypass thermal measuring principle, the Constant pressure heat capacity (C_p) and normal density of the gas (for a given pressure and temperature) allow for a conversion factor to be calculated, so to achieve a desired mass flow of CO₂, the conversion factor is applied to set the flow of the CO MFC to think it is still CO flowing, but in reality, the flow is 2ln/min of CO₂. As a result using the conversion factors between CO and CO₂ allow for the desired CO₂ mass flow to be achieved by setting the corresponding equivalent mass flow in terms of CO. Conversion factors are all referenced to a common reference gas, Air.

$$\frac{\text{Gas Flow}_1}{\text{CF}_1(C_{p,1}, \rho_1)} = \frac{\text{Gas Flow}_2}{\text{CF}_2(C_{p,2}, \rho_2)} \quad (\text{A1})$$

Where,

CF ₁	Conversion factor from Gas 1 to Air
C _{p,1}	Constant pressure heat capacity of gas 1 ($\frac{J}{mol \cdot K}$)
ρ_1	Gas 1 density ($\frac{kg}{m^3}$)
CF ₂	Conversion factor from Gas 2 to Air
C _{p,2}	Constant pressure heat capacity of gas 2 ($\frac{J}{mol \cdot K}$)
ρ_2	Gas 2 density ($\frac{kg}{m^3}$)

Calibration was applied to 3 of the MFCs by the use of a Gilibrator (Sensidyne Gilian Gilibrator 2), to ensure for an appropriate working accuracy. For each of the MFCs, a series of programmed values were trialed from 0 ln/min up to 2 ln/min, recordings were measured using the MFC, and from the Calibrator were taken. N₂ gas was employed for the calibration procedure for each of the 3 mass flow controllers, as a result, 2 of the mass flow controllers are designed for an alternative gas (CO and H₂). Applying the conversion factors for each gas w.r.t Air allowed an equivalent mass flow conversion to be made to N₂ (using equation A1 above), this equivalent N₂ mass flow can then be compared to the N₂ Gilibrator mass flow readings. A series of mitigation methods were enforced to account for the zero value being incorrect, and general drift encountered when

increasing the flow rates. After calibration, the accuracy of the MAE for a target Mass Flow were improved by factors of; 8.7, 394.4, and 4.6 for the N₂, CO (CO₂), and H₂ MFCS respectively. The calibration procedure required zero offset adjustment, and a linear regression transformation to ensure accurate readings. Table A1 shows a comparison of the MAE between the true gas flow and the Bronkhorst mass flow measurements, before and after the calibration.

Table A1: Measured errors for the gas flow controllers represented by 2 standard deviations.

Bronkhorst Flow Controller	MAE Before Calibration (ml/min)	MAE After Calibration (ml/min)
N ₂ MFC	62.22	7.15
CO ₂ MFC	339.21	0.86
H ₂ MFC	30.43	6.66

Note the MAE prior to calibration for the CO₂ MFC was due to a significant error in the zero value.

Converting the CO MFC to output a desired flow rate of a target gas medium, a simple scaling factor transformation is used (Note 'setpoint' refers to the open valve position using Bronkhorst RS-232 ProPar communication through Python):

$$\text{Setpoint}_{CO} = \frac{\text{Desired Flow Rate} \times CF_{CO \rightarrow Air} \times 32000}{1.1 \times CF_{Target \rightarrow Air} \times 20} \quad (\text{A2})$$

Where,

- 32000 Setpoint_{max} using Bronkhorst ProPar communication (corresponding to 100% valve open)
- 20 Max flow rate (ln/min) for each MFC.
- 1.1 Correction scaling factor.

Converting the N₂ MFC to output a desired flow rate of a target gas medium, apply the linear transformation:

$$\text{Setpoint}_{N_2} = \frac{(\text{Desired Flow Rate} + 0.0199) \times CF_{N_2 \rightarrow Air} \times 32000}{1.1303 \times CF_{Target \rightarrow Air} \times 20} \quad (\text{A3})$$

Where,

- 32000 Setpoint_{max} using Bronkhorst ProPar communication.
- 20 Max flow rate (ln/min) for each MFC.
- 0.0199 Linear transformation bias.
- 1.1303 Linear transformation weight.

Converting the H₂ MFC to output a desired flow rate of a target gas medium, apply the linear transformation:):

$$\text{Setpoint}_{\text{H}_2} = \frac{(\text{Desired Flow Rate} + 0.0485) \times \text{CF}_{\text{H}_2 \rightarrow \text{Air}} \times 32000}{1.1286 \times \text{CF}_{\text{Target} \rightarrow \text{Air}} \times 20} \quad (\text{A4})$$

32000 Setpoint_{max} using Bronkhorst ProPar communication.

20 Max flow rate (ln/min) for each MFC.

0.0485 Linear transformation bias.

1.1286 Linear transformation weight.